JGR Space Physics

RESEARCH ARTICLE
10.1029/2019JA026540

Special Section:
Equatorial Aeronomy: New results from the 15th International Symposium on Equatorial Aeronomy (ISEA-15) and beyond

A New Artificial Neural Network-Based Global Three-Dimensional Ionospheric Model (ANNIM-3D) Using Long-Term Ionospheric Observations: Preliminary Results

V. Sai Gowtam[1], S. Tulasi Ram[1], B. Reinisch[2,3], and A. Prajapati[1]

[1]Indian Institute of Geomagnetism, Navi Mumbai, India, [2]Lowell Digisonde International, Lowell, MA, USA, [3]Center for Atmospheric Research, University of Massachusetts Lowell, Lowell, MA, USA

Key Points:
- A new artificial neural network-based 3-D ionospheric model (ANNIM-3D) using nearly two decades of global ionospheric data is presented
- The ANNIM-3D predictions are consistent with the ground-based Digisonde, incoherent scatter radar, and satellite in situ observations
- The ANNIM-3D can successfully reproduce EIA, annual anomaly, main ionospheric trough, and ionospheric response to geomagnetic activity

Correspondence to:
S. Tulasi Ram,
tulasi@iigs.iigm.res.in

Citation:
Gowtam, V. S., Tulasi Ram, S., Reinisch, B., & Prajapati, A. (2019). A new artificial neural network-based global three-dimensional ionospheric model (ANNIM-3D) using long-term ionospheric observations: Preliminary results. *Journal of Geophysical Research: Space Physics*, *124*. https://doi.org/10.1029/2019JA026540

Received 24 JAN 2019
Accepted 21 MAY 2019
Accepted article online 31 MAY 2019

Abstract In this paper, we present the preliminary results of a new global three-dimensional (3-D) ionospheric model developed using artificial neural networks (ANNs) by assimilating long-term ionospheric observations from nearly two decades of ground-based Digisonde, satellite-based topside sounders, and global positioning system-radio occultation measurements. The present 3-D model is named ANN-based global 3-D ionospheric model (ANNIM-3D), which is the extension of previous work on the ANN-based two-dimensional ionospheric model by Sai Gowtam and Tulasi Ram (2017a, https://doi.org/10.1002/2017JA024795) and Tulasi Ram et al. (2018, https://doi.org/10.1029/2018JA025559). The vertical electron density profiles derived from ANNIM-3D model are found to be consistent with the ground-based incoherent scatter radar observations at Jicamarca and Millstone Hill. The model results have been thoroughly validated and found in good agreement with the ground-based Digisonde and satellite in situ observations at different altitudes. This model successfully reproduces the large-scale ionospheric phenomena like diurnal and seasonal variations of equatorial ionization anomaly and its hemispheric asymmetries, ionospheric annual anomaly, and the main ionospheric trough. Also, the present model has predicted the ionospheric response that is consistent with the neutral composition changes and meridional wind circulations during disturbed geomagnetic activity periods. Finally, the merits and limitations of this model and the scope for the potential improvements have been discussed.

1. Introduction

The accurate determination of the ionospheric conditions is a crucial element to serve the ever increasing Satellite-Based Augmentation System needs. Since the ionosphere is a region sandwiched between the neutral-dominated lower atmosphere and the plasma-dominated outer space, the ionospheric plasma density is significantly influenced by various forces from both the lower atmospheric origin and direct solar control. Apart from production and loss, the plasma transport processes play a vital role in the spatial and temporal variability of the ionosphere. The electrodynamic drifts due to electric fields and collisional drag due to thermospheric neutral wind circulations in the presence of the Earth's magnetic field chiefly control the field-perpendicular and field-aligned plasma transport in the ionosphere. Further, the magnitude and polarity of these processes vary dramatically under disturbed space weather conditions. Since the first theoretical descriptions of the ionospheric layers by Chapman (1931a, 1931b), great efforts have been made across the world to model the ionosphere during the past seven decades. The present ionospheric models can be broadly classified into two categories as empirical and theoretical models. Empirical models use climatological ionospheric data from various observations and fit the ionospheric parameters with given set of control parameters using predefined analytical functions. For example, the International Reference Ionosphere (IRI; Bilitza, 2001, Bilitza & Reinisch, 2008; Bilitza et al., 2014, 2017) and NeQuick (Hochegger et al., 2000; Nava et al., 2006; Radicella & Leitinger, 2001) are widely used global empirical models for the three-dimensional ionosphere. Also, some interesting works on the development of two-dimensional ionospheric models on global and regional scales can be found in the literature. For example, Altadill et al. (2013) developed a global empirical model for the $F2$-layer peak height (h_mF2) and effective scale height for quiet geomagnetic conditions using spherical harmonic analysis. Zhang et al. (2014) have built a global empirical model for h_mF2 from ionosonde and global positioning system-radio occultation (GPS-RO) observations based on two-layer empirical orthogonal function analysis. Shubin

(2017) has reported a global *foF*2 model for quiet geomagnetic conditions using ionosonde and GPS-RO observations. Recently, Themens et al. (2017) have reported the new Empirical Canadian High Arctic Ionospheric Model for N_mF2 and h_mF2 over the Arctic region (>50°N geomagnetic latitudes). Physics-based theoretical models, on the other hand, solve the conservation (continuity, momentum, and transport) equations of individual constituents to predict the ionospheric variability in spatial and temporal domains. The Sheffield University Plasmasphere and Ionosphere Model (Bailey et al., 1997; Bailey & Balan, 1996), Thermosphere-Ionosphere-Electrodynamics General Circulation Model (Richmond et al., 1992; Roble et al., 1988), Coupled Thermosphere Ionosphere Model (Fuller-Rowell et al., 1996), and the SAMI2/SAMI3 is Another Model of Ionosphere (Huba et al., 2000; Huba et al., 2008) are some of the well-known theoretical models. With the advantages and limitations of these models, the accurate prediction of ionospheric variability under varied space weather conditions is still a challenging task due to various simultaneously operating dynamical processes and the complex nonlinear behavior of the ionosphere.

In recent times, the artificial neural networks (ANNs) and machine learning techniques have been used to solve the more complex problems, such as classification, clustering, control, decision making, nonlinear data fitting, and prediction. In ANN-based modeling, sufficiently large data sets are trained with a set of inputs to get a nonlinear input-output relationship. The utilization of ANNs in ionospheric and magnetospheric studies is steadily increasing with time. For example, the prediction of ionospheric peak height (h_mF2), peak density/critical frequency of ionosphere (N_mF2/*foF*2), total electron content, sunspot number, and interplanetary conditions using ANNs can be found in the literature (Athieno et al., 2017; Clausen & Nickisch, 2018; Hu & Zhang, 2018; Huang & Yuan, 2014; Kumluca et al., 1999; Lamming & Cander, 1999; Oyeyemi et al., 2005; Oyeyemi & Poole, 2004; Poole & Poole, 2002; Watthanasangmechai et al., 2012; Wintoft, 2000; Xenos, 2002; Zhao et al., 2014; Zhelavskaya et al., 2016). These studies demonstrate the ability of ANNs to model and predict the ionospheric and the magnetospheric parameters under various geomagnetic conditions. However, most of these studies aimed to develop a neural network-based model to predict the ionospheric parameters at a given location or region with a limited number of observations. However, with the availability of globally distributed long-term data sets from various GPS-RO, ground-based Digisondes, and topside sounder observations, it is now possible to develop a global ionospheric model using ANNs. Recently, an ANN-based global two-dimensional ionospheric model (ANNIM) was developed to predict the N_mF2 and h_mF2 by utilizing the long-term data from Formosa Satellite-3/Constellation Observing System for Meteorology, Ionosphere and Climate (FORMOSAT-3/COSMIC) radio occultation mission (Sai Gowtam & Tulasi Ram, 2017a). Later, Tulasi Ram et al. (2018) improved ANNIM by assimilating additional data from the Digisonde Global Ionosphere Radio Observatory (GIRO, Reinisch & Galkin, 2011), CHAMP and GRACE (Gravity Recovery And Climate Experiment) radio occultation measurements and modified gridding approach. Through the controlled simulations, Tulasi Ram et al. (2018) have shown that the ANNIM could successfully distinguish the roles of recurrent geomagnetic activity and solar irradiance on ionospheric variability. The present work is the extension of the previous works by Sai Gowtam and Tulasi Ram (2017a) and Tulasi Ram et al. (2018) in developing a new three-dimensional (latitude, longitude, and altitude) ionospheric model based on ANNs (hereafter, ANNIM-3D) by using long-term ionospheric observations. The main objective of this study is to assess the ANN architecture and the methods used in this model development and to present the preliminary results of ANNIM-3D. The organization of the present paper is as follows. The data sets assimilated in the model and data preparation are described in section 2. The adopted methodology including the ANN architecture, training, and profiling the vertical electron density variation are presented in section 3. The validations of ANNIM-3D results with ground-based Digisondes, incoherent scatter radars (ISRs), and satellite in situ measurements at different altitudes are presented in sections 4.1–4.3. The ANNIM-3D simulations of large-scale ionospheric phenomena such as diurnal and seasonal variations of equatorial ionization anomaly (EIA), main ionospheric trough, and the ionospheric response during quiet and disturbed geomagnetic periods are discussed in sections 4.4–4.6. Finally, the merits and limitations of this model along with the scope for future improvements are summarized in section 5.

2. Data

The quantum of GPS-RO, Digisonde, and topside sounder data assimilated in the development of the present model is presented in Figure 1. This database from 1971 to 2016 spreads over different epochs of solar cycles 20 to 24 with a major portion of observations from solar cycles 23 and 24. The daily *F*10.7 solar flux variation

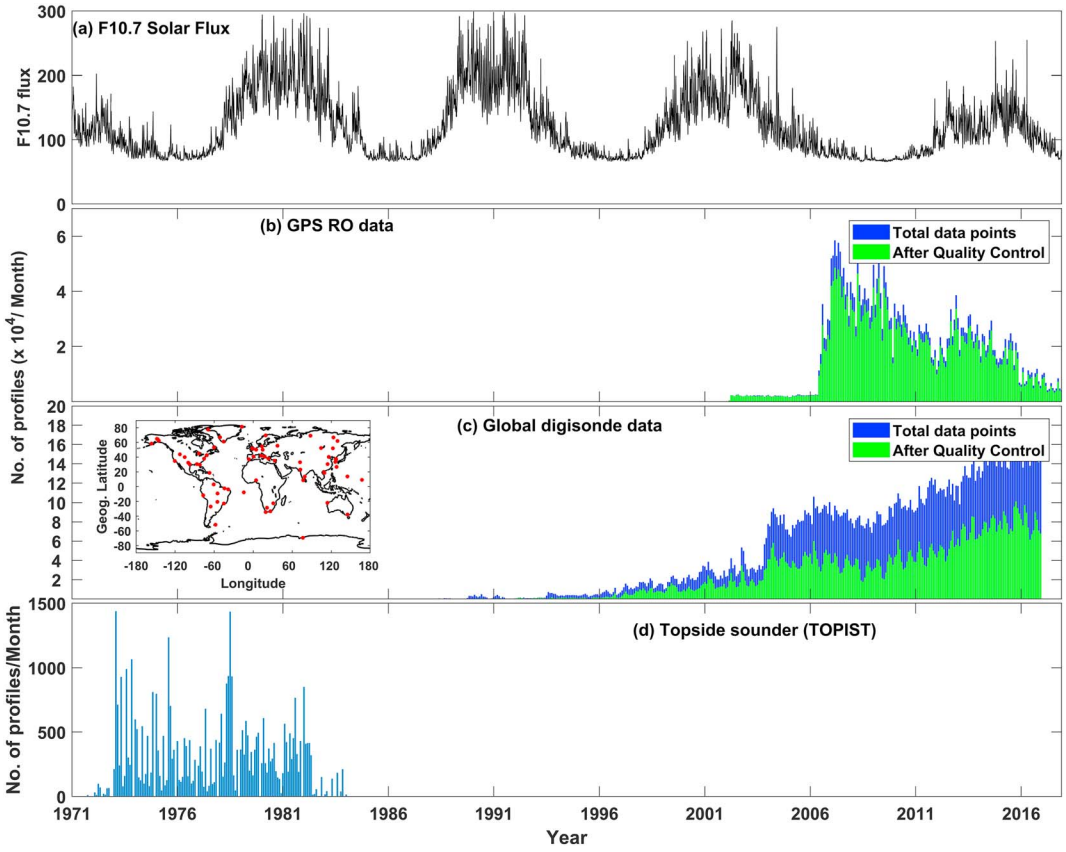

Figure 1. Quantum of data assimilated in artificial neural network-based global three-dimensional ionospheric model. (a) The daily variation of *F*10.7 solar flux from 1971 to 2016. (b) Number of global positioning system-radio occultation (GPS-RO) profiles per month from CHAMP, GRACE, and FORMOSAT-3/COSMIC together. (c) Number of bottomside profiles per month from GIRO-Digisonde network. The locations of the Digisonde stations considered in the study can be seen in the inset of Figure 1c. The blue bars (in Figures 1b and 1c) indicate the total number of electron density profiles per month, and the green bars represent the electron density profiles after the quality control measures. (d) The total number of electron density profiles per month from the topside sounders onboard International Satellites for Ionospheric Studies satellites.

from 1971 to 2016 is shown in the top panel (Figure 1a). The GPS-RO observations provide the electron density profile (Ne(h)) as a function of tangent point altitude from the satellite orbital altitude to ground (Rius et al., 1998; Schreiner et al., 1999; Syndergaard et al., 2006). The present study considers the electron density profile data from the GPS-RO missions FORMOSAT-3/COSMIC (2006-2016), CHAMP (2002-2008), and GRACE (2007-2015), provided by the University Center for Atmospheric Research (UCAR; available at https://cdaac-www.cosmic.ucar.edu/). The RO-retrieved vertical electron density profiles were found to exhibit good correlation with the ground-based ionosonde and ISR measurements (Lei et al., 2007; Schreiner et al., 2007). The GPS-RO profiles provide more or less uniform spatial coverage all over the globe including the large oceanic and inaccessible regions. In order to avoid noisy and fluctuating profiles, we have applied a three-step quality control as recommended in Yang et al. (2009), Potula et al. (2011), and Uma et al. (2016). In the first step, RO profiles with an average standard deviation greater than 1.5 are treated as "noisy profiles" and are removed. Second, the unusual RO profiles with h_mF2 greater than 550 km and some profiles with strong enhancements in *E* region densities are omitted, since they may be influenced by strong sporadic *E* layers. Some of the retrieved electron density profiles show negative electron density values that are unreal, and hence, they are removed from the analysis in the third step. Figure 1b shows the number of GPS-RO electron density profiles per month, from CHAMP, GRACE, and FORMOSAT-3/COSMIC together. The blue bars indicate the total number of profiles, and the green bars indicate the number of profiles after applying the discussed quality control measures.

Further, the bottomside electron density profile data from the ground-based Digisonde GIRO for the period from 1997 to 2016 were also considered. The GIRO is a network of Digisondes installed at 100+ locations

across the world (Reinisch et al., 2009; Reinisch & Galkin, 2011). The locations (geographic latitude and geographic longitude) of the Digisonde stations considered are shown in the inset of Figure 1c. The Digisonde ionograms are automatically scaled and the bottomside true height electron density profiles are computed using the Automatic Real-Time Ionogram Scaler with True height (ARTIST-5) software (Galkin et al., 2008). The bottomside true height profile data from the GIRO Digisonde network are downloaded using the Standard Archive Output (SAO) Explorer application from the Digital Ionogram Data Base (DIDBase) web portal (http://umlcar.uml.edu/DIDBase/). In the present study, the bottomside profiles with the confidence score below 90 are discarded to avoid scaling errors due to noisy ionogram traces and spread-*F* echoes. The blue bars in Figure 1c represent the total number of bottomside profiles per month extracted from the GIRO Digisonde network, and the profile data with confidence score greater than or equal to 90 are indicted by green bars. Further, we have also assimilated the topside sounders data from the United States/Canadian International Satellites for Ionospheric Studies satellites for the period from 1971 to 1984. The ionograms from the topside sounders were converted into topside electron density profiles using the Topside Ionogram Scaler with True height Algorithm (TOPIST) software (Benson, 2010; Bilitza et al., 2004; Huang et al., 2002). The total number of topside electron density profiles per month is shown in Figure 1d. These data were acquired from the National Aeronautics and Space Administration's Space Physics Data Facility center (https://nssdcftp.gsfc.nasa.gov/). The daily averaged values of *F*10.7 solar flux and 3-hourly *Kp* index have been obtained from National Aeronautics and Space Administration's space physics data facility (https://omniweb.gsfc.nasa.gov/). It should be mentioned here that the electron density profiles from different sources (GPS-RO from Format-3/COSMIC, GRACE, CHAMP, GIRO-Digisonde, and Topside Ionogram Scaler with True height Algorithm) cover different altitude regions of the ionosphere. However, the combined data set provides sufficiently dense observations between 150- and 700-km altitudes after applying the quality control.

To validate the model results, we have also used the vertical electron density profiles measured by the ground-based ISRs at Jicamarca (11.95°S, 76.87°W) and Millstone Hill (42.62°N, 71.49°W), and in situ electron density measurements from ROCSAT-1, CHAMP, and SWARM-A satellites. The first scientific satellite of Republic of China, ROCSAT-1, launched in 1999 into an inclined (35°) circular orbit at an altitude of ~600 km, measured the ion density using the Ionospheric Plasma and Electrodynamics Instrument (IPEI). CHAMP was launched in May 2000 into a circular polar orbit at an altitude of 455 km, and the orbit slowly descended to 300 km in 10 years. The SWARM (European Space Agency Magnetic Field Mission) is a constellation of three satellites (SWARM-A, SWARM-B, and SWARM-C), launched by the European Space Agency into a circular orbit at an altitude of 460 km. CHAMP and SWARM measure the in situ electron density using the onboard planar Longmuir probe. In the present study, in situ plasma density observation from ROCSAT-1, CHAMP during March 2004, and SWARM-A during March 2016 are considered for comparison with ANNIM-3D results.

3. Method of Model Construction

In the present study, globally distributed vertical electron density profiles from GPS-RO missions, GIRO-Digisonde network (bottomside only), and the topside sounder data are divided into 840 small spatial grids from −180°W to 180°E at 15° longitude and −87.5°S to 87.5°N at 5° dip latitude intervals. The architecture of ANNs used in the present work is shown in Figure 2. The controlling input parameters of ANNs (Figure 2a) are date (DD/MM/YYYY) or day of the year (DOY), universal time (UT), geographic latitude (ϕ), geographic longitude (λ), altitude (h), daily *F*10.7 solar flux, and 3-hourly *Kp* index. These primary inputs also flow to the International Geophysical Reference Field (IGRF-12; Thébault et al., 2015) and Horizontal Wind Model (HWM-14; Drob et al., 2015) to compute the declination, inclination, dip latitude, and zonal and meridional winds through internal subroutines indicated by the blues boxes (Figure 2b). The additional parameters computed from IGRF and HWM models are also fed to the ANNs to improve the functionality of the model and better learning of neural networks. The output layer (target) of the neural network is the electron density, which is a function of given input parameters. For the neural networks training, we have implemented the feed-forward neural network with Levenberg-Marquardt algorithm since it has excellent ability to handle complex problems with the fastest convergence rate (Hagan & Menhaj, 1994; Levenberg, 1944; Marquardt, 1963; Rumelhart et al., 1986). Figure 2c represents the architecture of the ANN used in the ANNIM-3D. The neural network in the present study has one input layer (with 12 input nodes), one

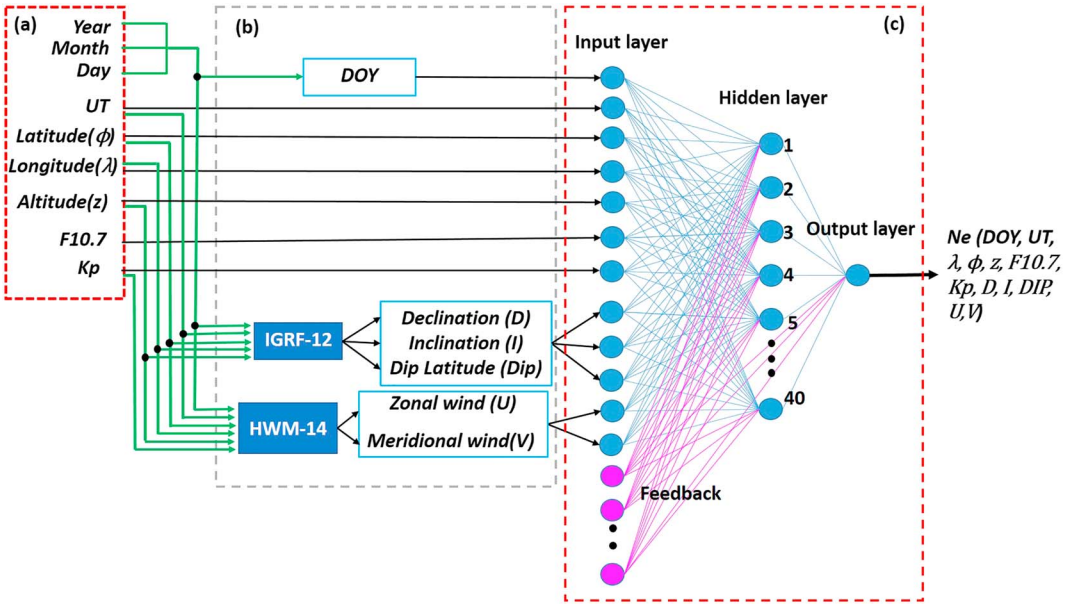

Figure 2. Architecture of the feed-forward neural network used in artificial neural network-based global three-dimensional ionospheric model. DOY = day of the year; UT = universal time.

hidden layer with 40 neurons, and one target layer (electron density). The electron density data between 150- and 700-km altitudes in each spatial grid are separately trained with the same neural network architecture. About 70% of data in each spatial grid is used for training the neural network, and the remaining 30% of data is used for validation and testing purposes. In general, the neural network architecture and the learning procedure implemented in this study are similar to that in Tulasi Ram et al. (2018), which gives further details. In the end, a total of 840 trained neural networks are combined through a front-end subroutine to construct a global three-dimensional ionospheric model that can initially predict the vertical electron density profile between 150- and 700-km altitudes for the given inputs shown in Figure 2. The initially predicted profile is then extrapolated up to 1,000 km in the topside and down to 70 km in the bottomside using another internal subroutine as described in the following paragraphs.

The vertical electron density variation in the topside ionosphere is usually expressed by analytical functions, such as exponential, parabolic, α-Chapman, and Epstein functions (Booker, 1977; Di Giovanni & Radicella, 1990; Rawer et al., 1985; Rawer, 1988; Reinisch & Huang, 2001; Reinisch et al., 2004, 2007; Stankov et al., 2003; Bilitza et al., 2006; Tulasi Ram, Su, Liu, Reinisch, et al., 2009). One of the important parameters in all these analytical functions is the topside scale height (H_T), which determines the shape of the electron density profile. In the present model, we have adopted the α-Chapman function (Hargreaves, 1979, 1992) to extrapolate the topside profile up to 1,000 km, which is given by the following equation.

$$Ne\,(h) = N_m\mathrm{F2}.\exp(0.5*(1-z-e^{-z})) \text{ with } z = \frac{(h-h_m F2)}{H_T}, \tag{1}$$

where N_mF2 and h_mF2 are the density and height of the $F2$-layer peak and H_T is the topside effective scale height. As mentioned above, the model can initially predict the electron density profile between 150 and 700 km from which N_mF2 and h_mF2 are obtained, and H_T is derived by least squares fitting the initial profile between h_mF2 and h_mF2 + 200 km using the equation (1). Similarly, we have used an IRI function (Bilitza et al., 2014) to extrapolate the bottomside electron density profile down to 70 km, which is given by

$$Ne\,(h) = N_mF2.\frac{\exp\left(-Z^{B_1}\right)}{\cosh(Z)}, Z = \frac{(h_mF2-h)}{B_0}, \tag{2}$$

where B_0 and B_1 are the thickness and shape parameters, respectively. B_1 is derived from the analytical fit between h_mF2 and the height where the bottomside density is 0.24 × N_mF2 (similar to Bilitza et al., 2014) or 150 km, whichever is less. Thus, by deriving the N_mF2, h_mF2, H_T, B_0, and B_1 from the model-predicted

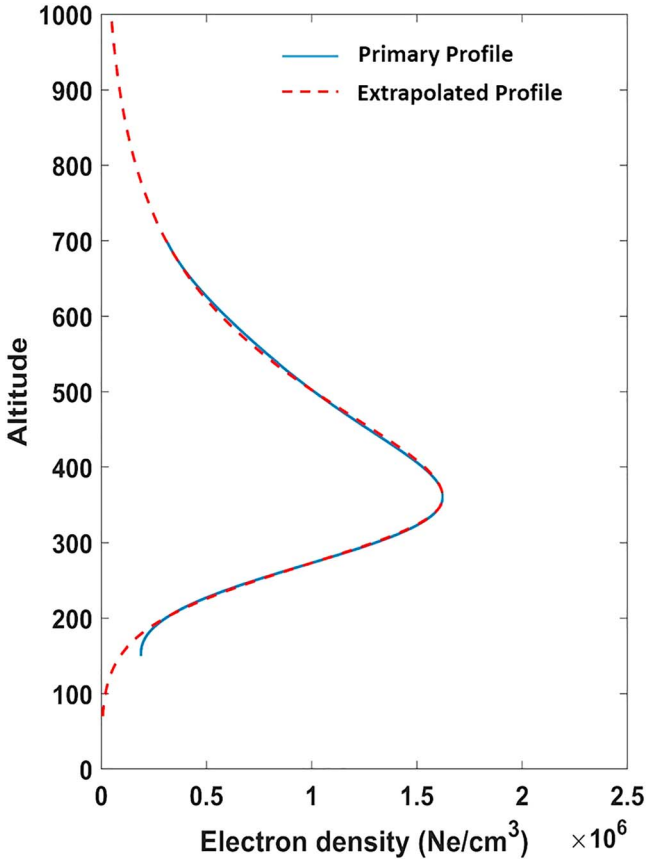

Figure 3. The typical example of initial vertical electron density profile data (Ne (h)) predicted by artificial neural network-based global three-dimensional ionospheric model between 150 and 700 km (blue solid curve) and the extrapolated Ne profiles using the analytical functions (red dashed curve). Please refer text for more details.

primary profile, one can extrapolate the vertical electron density profile between 70 to 1,000 km using the equations (1) and (2). For example, the blue solid curve in Figure 3 represents the primary vertical electron density profile predicted by the model between 150 and 700 km. The topside electron density is extrapolated using the α-Chapman function, and the bottomside is extended using the IRI equation as explained above to get the vertical electron density profile between 70 and 1,000 km. The red dashed curve in Figure 3 represents the vertical electron density profile after the extrapolations.

4. Results and Discussion

In this section, the preliminary results of the ANNIM-3D model are presented in comparison with ground-based Digisonde, ISRs, and satellite in situ observations alongside the empirical IRI 2016 model. The ANNIM-3D simulations of diurnal and seasonal variations of EIA, main ionospheric trough, and ionospheric response to quiet and disturbed geomagnetic conditions are presented and discussed in this section.

4.1. Comparison With Digisonde Observations at Different *F*10.7 Solar Flux Conditions

With a view to examine the ANNIM-3D response under variable solar activity conditions, the vertical electron density profiles have been simulated at an equatorial location, Jicamarca (11.95°S, 76.8°W and 0.7°N dip latitude), and a midlatitude station, Grahamstown (33.3°S, 26.5°E and 46.5°S dip latitude), for different *F*10.7 solar flux inputs at 12 local time under March equinox conditions (DOY = 81). Figure 4a shows the variations in the vertical electron density profile at Jicamarca for *F*10.7 solar flux variations from 60 to 220 sfu (solar flux units, 1 sfu = 10^{-22} W·m^{-2}·Hz^{-1}). It can be observed that the *F*10.7 dependence is well captured by the ANNIM-3D. Both the electron density and the height of the *F*-layer peak are found to increase with the increasing solar activity. Figures 4b and 4c show the N_mF2 and h_mF2 variation from the ANNIM-3D profiles as a function of *F*10.7 solar flux (red curves). The blue solid circles in the Figures 4b and 4c are the actual N_mF2 and h_mF2 observations from the collocated Digisonde at Jicamarca. It can be seen from these figures that both N_mF2 and h_mF2 increase with the solar flux, matching well with the collocated Digisonde observations. A careful observation of Figure 4a reveals another interesting feature that the bottomside height and the steepness of the profile between 150 and 350 km increase with increasing solar activity. Further, the topside profile becomes broader with increasing *F*10.7. As Jicamarca being an equatorial location, the shape of the vertical electron density profile is largely influenced by the primary dawn-dusk electric field through vertical E × B drift. The vertical motion of plasma through E × B drift causes the elevation of equatorial *F* layer and steepens the profile as observed in Figure 4a. The E × B drift also influence the topside scale height leading to the broadening of the profile with increasing solar activity (Tulasi Ram, Su, Liu, Reinisch, et al., 2009). It is reassuring to see that these solar activity-dependent and E × B drift-related variations in the shape of the vertical electron density profiles have been well captured by the ANNIM-3D despite the absence of a zonal electric field input. This indicates that these features that exist in the database have been captured by the model through systematic learning of ANNs. Figures 4d–4f show similar vertical electron density profile variations with *F*10.7 solar flux and comparison of N_mF2 and h_mF2 with collocated Digisonde observations at a midlatitude station, Grahamstown. Both the N_mF2 and h_mF2 increase with increasing solar activity and exhibit good correspondence with the collocated Digisonde observations (Figures 4e and 4f).

The results presented in Figure 4 indicate that the ANNIM-3D can well reproduce the solar activity-dependent variations for *F*10.7 varying between 60 and 220 sfu. However, as shown in Figure 1, the majority of the GPS-RO data considered in this study comes from the FORMOSAT-3/COSMIC mission from the year

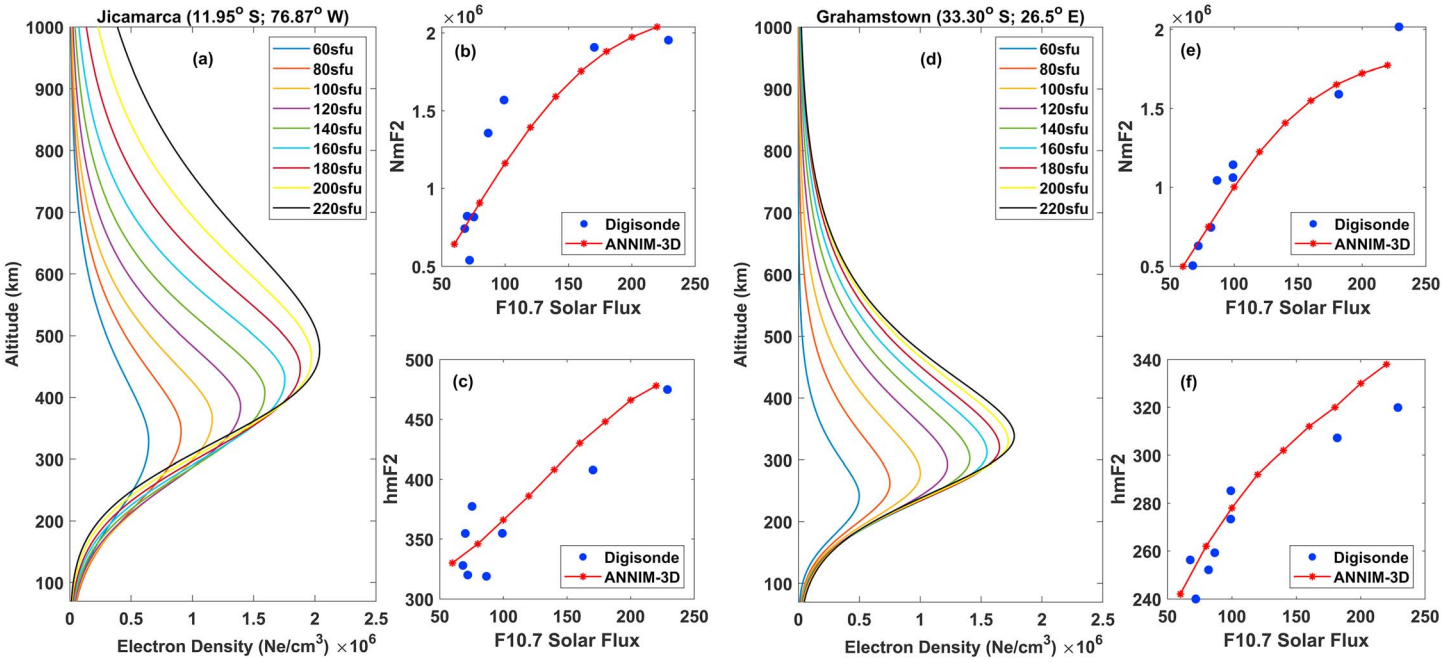

Figure 4. Vertical electron density profiles for 12 local time under March equinox conditions, simulated by ANNIM-3D for varying *F*10.7 solar flux inputs and comparisons of N_mF2/h_mF2 with collocated Digisonde observations at an equatorial location, Jicamarca (a–c) and a midlatitude station, Grahamstown (d–f). ANNIM-3D = artificial neural network-based global three-dimensional ionospheric model.

2006 and later. This period belongs to the solar minimum to moderate solar maximum of solar cycle 24. Further, the major portion of GIRO-Digisonde data also covers solar minimum to moderate maximum of solar cycle 24. This low to moderate solar activity weightage in the GPS-RO and GIRO-Digisonde data may impact the model performance at very high *F*10.7 solar flux conditions (above 220 sfu).

4.2. Comparison With ISR Observations at Jicamarca and Millstone Hill

The vertical electron density profiles predicted by ANNIM-3D at Jicamarca for different local times have been compared with the Jicamarca ISR observations. For this purpose, we have considered 2 days of vertical profile observations during 6 and 7 March 2013 from the Faraday rotation long-pulse experiment (Hysell, 2000; Hysell et al., 2008) with the Jicamarca radar system. For example, Figure 5a compares ANNIM-3D-predicted profiles (blue curves) with ISR profiles (red curves) at 3-hr local time intervals. The IRI 2016 model-predicted profiles (green curves) are shown for comparison. The difference between model predictions and ISR observations expressed in percentage ($\Delta Ne\ \% = ((\text{model profile} - \text{ISR profile})/\text{ISR profiles}) \times 100$) are shown in the insets on the rightside of each panel using the same color code. It can be seen from this figure that the ANNIM-3D-predicted profiles are in general agreement with the Jicamarca ISR profiles at all local times with reasonable deviations that are usually expected for a model result when compared with measured data, and the same is the case for IRI 2016 model predictions as well. The ANNIM-3D-predicted electron density profiles exhibit good similarity with the ISR profiles at most local times, except in postmidnight to predawn hours (00–06 LT) where the ANNIM-3D significantly overestimates the electron density. It should be noted that the large ΔNe (greater than 300%) at local times and at altitudes where the ISR electron density is very low due to the normalization by the background electron density in the denominator while computing the percentage deviation. Nevertheless, the ΔNe in ANNIM-3D profiles are relatively small compared to the IRI 2016 profiles except during postmidnight hours (00–03 LT).

Similarly, the ANNIM-3D electron density profiles have been compared with ISR observations at a midlatitude station, Millstone Hill (48.62°N, 71.49°W), at different local times as shown in Figure 5b. One can see that the ANNIM-3D-predicted profiles agree well with the Millstone Hill ISR profiles at all local times except in predawn hours (03–06 LT) where the ANNIM-3D overestimates the electron density. The percentage deviations (ΔNe) in the ANNIM-3D predictions are very small around *F*2-region altitudes (200–500 km).

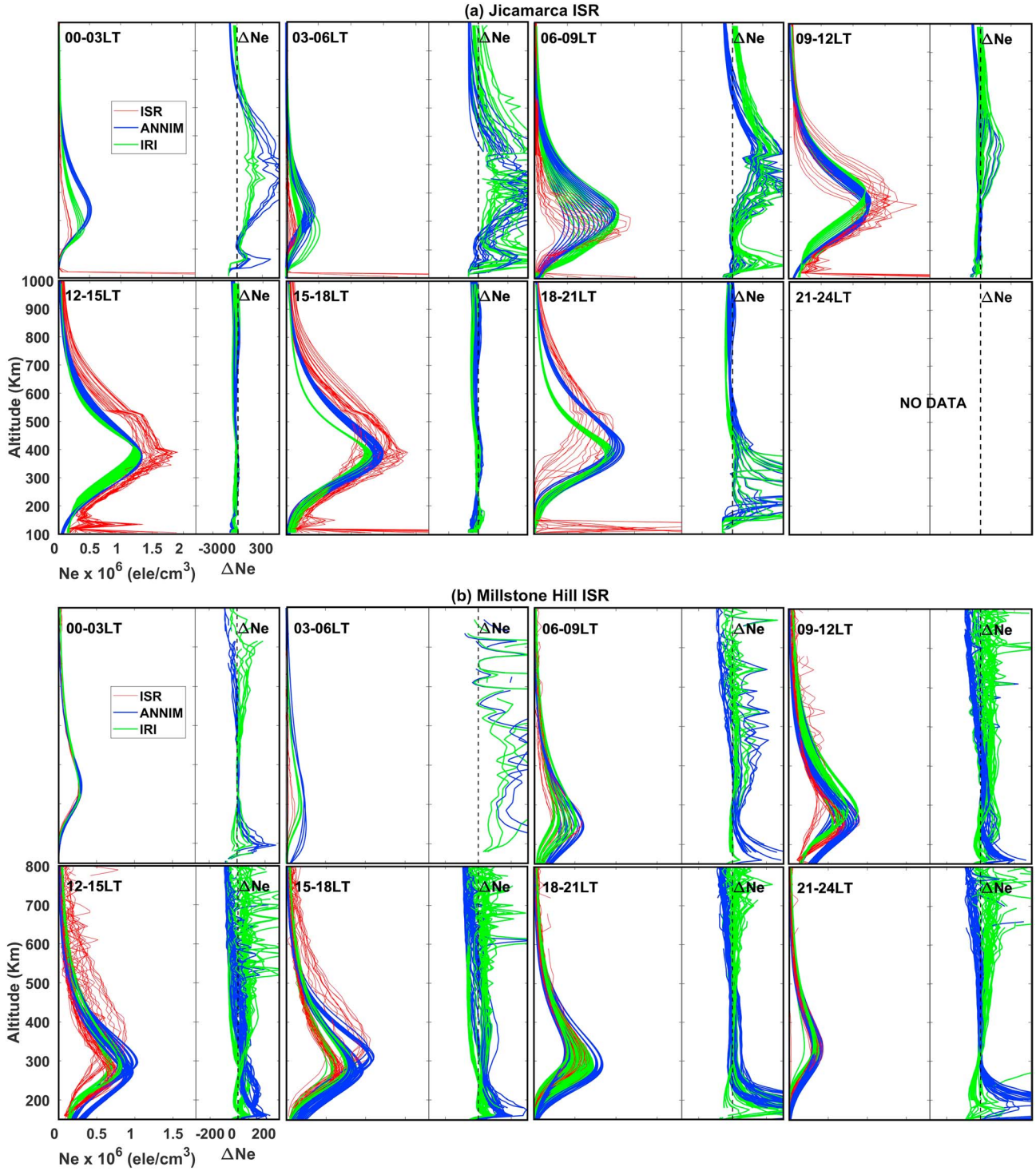

Figure 5. Comparison of artificial neural network-based global three-dimensional ionospheric model-predicted electron density profiles (blue curves) with ground based ISR profiles (red curves) at Jicamarca (Figure 5a) and Millstone Hill (Figure 5b) during March 2013. The IRI 2016-predicted (green curves) profiles have also shown for comparison. The percentage of deviations in the model predictions with respect to ISR observations (ΔNe % = ((model Ne − ISR Ne)/ISR Ne) × 100) were shown in the right-hand side insets in each panel using the same color scheme. ISR = incoherent scatter radar.

However, the ΔNe values show a systematic overestimation at altitudes below 200 km and slight underestimation above 500 km by ANNIM-3D at all local times. On the other hand, the IRI 2016 (green curves) exhibits an overestimation in the topside ionosphere (above 500 km).

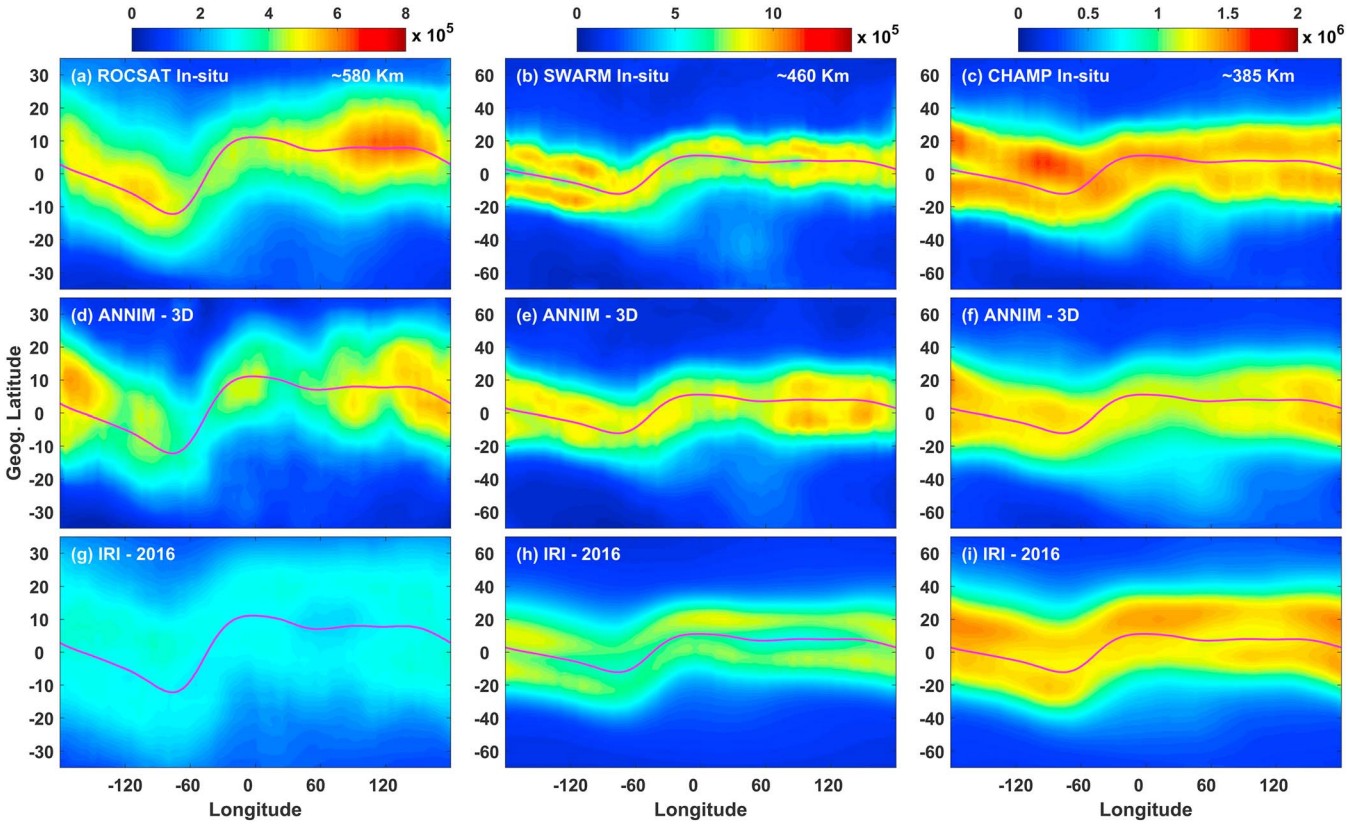

Figure 6. The global electron density maps constructed at local noon (12 LT ± 1 hr) using topside in situ measurements (top panels) from ROCSAT-1 (580 km), SWARM-A (460 km), and CHAMP (385 km) satellites. The middle and bottom panels present the global electron density maps simulated using ANNIM-3D and IRI 2016 models, respectively, under the same conditions as satellite observations. The magenta curves in each panel indicate the dip equator. ANNIM-3D = artificial neural network-based global three-dimensional ionospheric model; IRI = International Reference Ionosphere.

In general, the comparisons with the ISR profiles at equatorial latitudes (Jicamarca) and midlatitudes (Millstone Hill) shown in Figures 5a and 5b indicate that the ANNIM-3D predictions are reasonably good with deviations that are expected when the model results are compared with observations. It should be noted that one of the major sources of deviations is the day-to-day variability of the ionosphere that is present in the observations while the model can predict only the average state of the ionosphere for the given set of input conditions. Nevertheless, the percentage deviations in the ANNIM-3D predictions are only slightly smaller compared to IRI 2016 model predictions for Jicamarca and nearly equal for Millstone Hill. This indicates that the performance of ANNIM-3D is as good as the IRI 2016 model. However, one notable limitation of this model is the overestimation of electron density at midnight to predawn hours at both locations.

4.3. Comparison With Satellite In Situ Observations

The in situ measured plasma densities from three satellites (ROCSAT-1, SWARM-A, and CHAMP) orbiting at three different altitudes in the topside ionosphere were considered for comparison with the ANNIM-3D, and the results are presented in Figure 6. The ROCSAT-1 and CHAMP in situ data correspond to the year 2004, whereas the SWARM-A data correspond to the year 2016. The orbital altitudes of ROCSAT-1, SWARM-A, and CHAMP during the periods of study are ~580, 460, and 385 km, respectively. In order to construct the global electron density distribution maps, the in situ data for a 40-day window centered on the March equinox (day number 80 ± 20 days) were binned into 5° geographic longitude × 2.5° geographic latitude bins and averaged. For example, Figures 6a–6c (top panels) show the global local noon (12 LT) plasma density distributions from ROCSAT-1 (580 km), SWARM-A (460 km), and CHAMP (385 km), respectively. The middle panels (Figures 6d–6f) show the model-predicted electron density distributions for the same input (day number, UT, latitude, longitude, $F10.7$, and Kp) conditions as for the satellite in situ

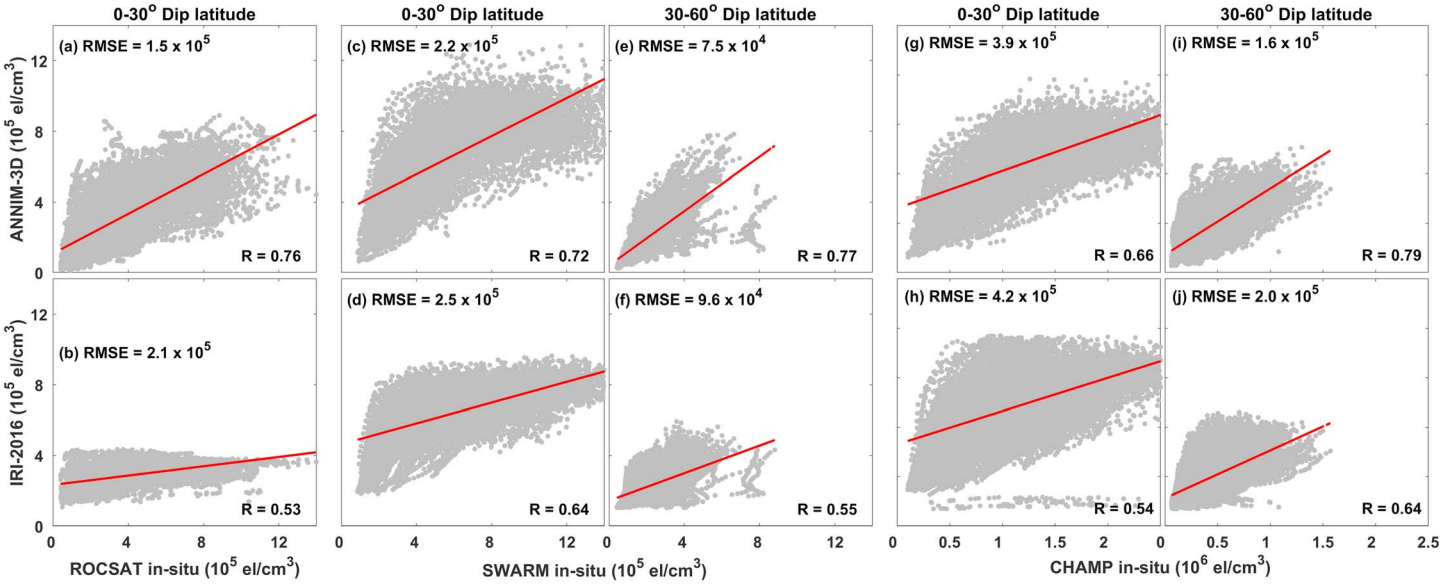

Figure 7. The comparisons of ANNIM-3D-predicted (top panels) and IRI 2016-predicted (bottom panels) electron density values with satellite in situ observations by ROCSAT-1 (a, b), SWARM (c–f) and CHAMP (g–j) at low and middle latitudes. The red straight lines indicate the linear regression between the ANNIM/IRI predictions and in situ data. ANNIM-3D = artificial neural network-based global three-dimensional ionospheric model; IRI = International Reference Ionosphere.

data. The bottom panels (Figures 6g–6i) show similar electron density distributions simulated from IRI 2016 model for comparison.

One can see from this figure that the electron density values predicted by the ANNIM-3D (Figure 6d–6f) are generally comparable with the satellite in situ measurements by ROCSAT-1 (Figure 6a), SWARM (Figure 6b), and CHAMP (Figure 6c). Further, the spatial (longitudinal and latitudinal) variation of the electron density is well represented by this model. On the other hand, the topside electron density values around 580 and 460 km are generally underestimated by the IRI 2016 model compared to the in situ observations of ROCSAT-1 and SWARM-A, respectively. The electron density values predicted by the ANNIM-3D and IRI 2016 are nearly comparable around CHAMP orbit (~385 km), which is close to the *F*2 peak. However, the IRI 2016 better represents the electron density distribution at this altitude; for example, the low-latitude electron densities over African and Asian (0–100°E) longitudes is underestimated by the ANNIM-3D compared to the IRI 2016.

Figure 7 shows the comparisons of ANNIM-3D-predicted (top panels) and IRI 2016-predicted (bottom panels) electron densities with satellite in situ observations by ROCSAT-1 (a, b), SWARM (c–f), and CHAMP (g–j). The comparisons are shown separately for the low latitudes (0° to ±30° dip latitudes) and midlatitude (±30° to ±60° dip latitudes) as indicated at the top of the panels. Since the ROCSAT-1 is a low-inclination (35°) orbiting satellite, only comparisons at low latitudes have been presented. The red straight lines indicate the linear regression between the ANNIM/IRI predictions and in situ data. The regression coefficients (*R*) and RMSE between the model predictions and in situ observations are indicated in each panels. Figure 7 shows that the model-predicted Ne exhibits good correlation with the satellite in situ observations. The regression coefficient (*R*) is varying between 0.66 to 0.79 for ANNIM and 0.53 to 0.64 for IRI 2016. One can notice that the ANNIM-3D predictions exhibit slightly better regression coefficients and smaller RMS errors than IRI 2016 with respect to the in situ data, particularly in the topside ionosphere where the IRI 2016 found to underestimate the electron density and tends to saturate at lower values. Nonetheless, from Figures 6 and 7, one can conclude that the ANNIM-3D predictions compare well with the satellite in situ observations at the three different altitudes.

4.4. Diurnal Evolution and Seasonal Variations of EIA

The temporal evolution of EIA over the Indian (75°E) longitude sector during moderate solar activity ($F10.7 = 120$ sfu) and quiet geomagnetic ($Kp = 1$) conditions was simulated using ANNIM-3D. Figure 8a shows the latitude and altitude distribution (longitudinal cut) of electron density at 3-hr local

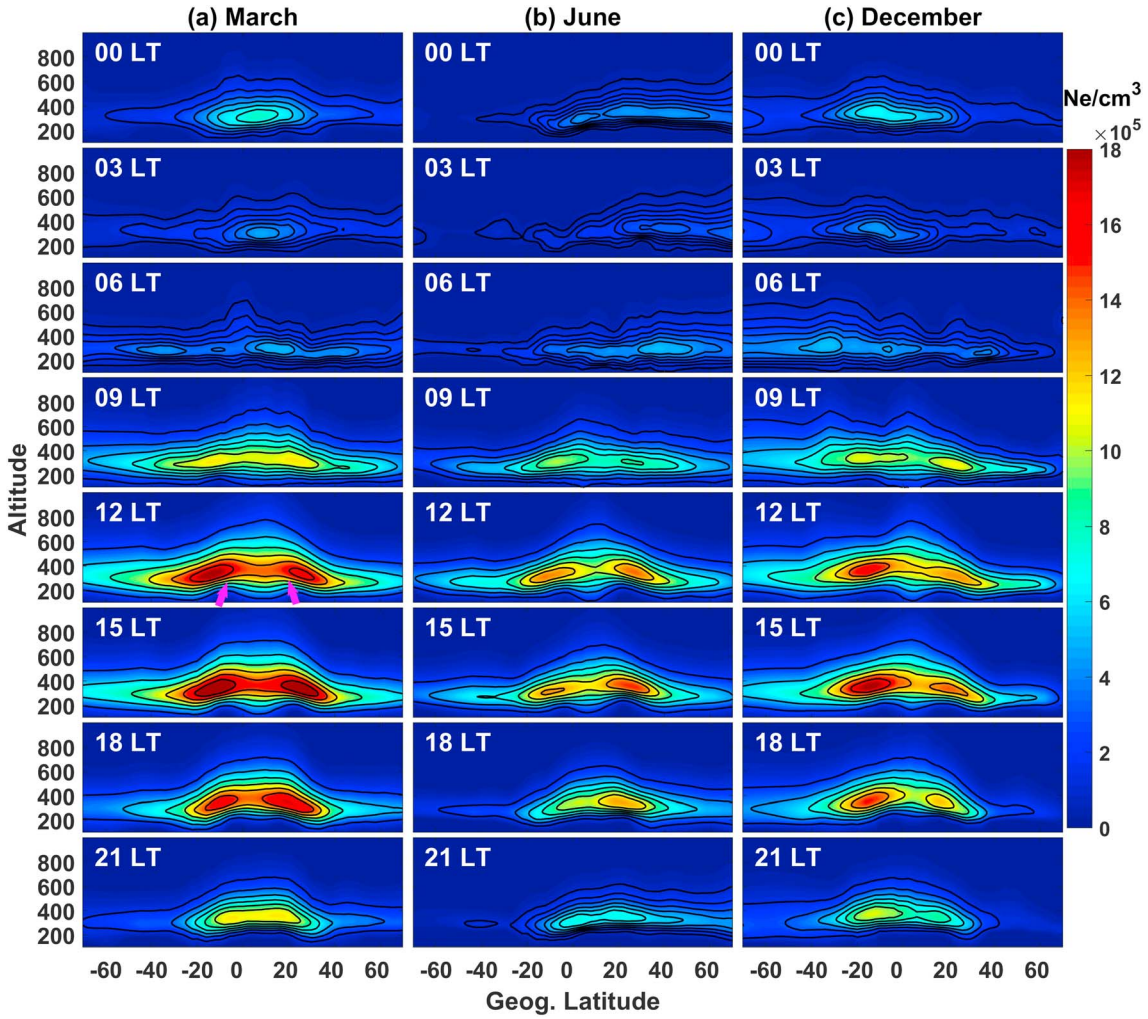

Figure 8. The altitudinal and latitudinal distributions of the electron density simulated using ANNIM-3D at every 3-hr local time intervals under moderate solar activity conditions ($F10.7 = 120$ sfu) during March equinox (Figure 8a), June (Figure 8b), and December (Figure 8c). The pink arrows in the panel corresponding to 12 LT in Figure 8a indicate the artificial plasma caves.

time intervals during the March equinox (day number = 80). It can be noticed from this figure that the ionization in the *F* region starts building around 6 LT, which is due to photoionization by the solar radiation. The small peaks of ionization around ~15°N and ~40°S at 6 LT could be due to action of neutral winds. However, there is no clear signature of the EIA until 9 LT. Around 9 LT, the ionization at the dip equator is depleted and transported toward low latitudes due to the so-called equatorial plasma fountain process, leading to the formation of double ionization crests away from the dip equator. At 12 LT, one can notice a well-developed EIA around the equatorial and low-latitude region. The altitudes of the EIA crests are more or less similar in both Northern and Southern Hemispheres. Further, the EIA is maintained throughout the afternoon hours and gradually suppressed after sunset. After 21 LT, the EIA is completely absent with only one peak of electron density being maintained in the equatorial region from midnight to predawn hours.

Figures 8b and 8c show similar latitudinal and altitudinal distribution of electron density predicted by ANNIM-3D during June and December solstices at 3-hr local time intervals over the Indian (75°E) sector. It can be noticed from Figure 8b that during June solstice, the ionization starts building first in the Northern Hemisphere around 6 LT because of early sunrise in the summer (Northern) hemisphere. A small peak in electron density around 40°N may be due to the action of neutral winds. Around 9 LT one can see the formation of EIA with two electron density peaks away from the dip equator with a slightly stronger EIA

crest in the winter (Southern) hemisphere. Interestingly, the EIA crest in the summer hemisphere becomes stronger compared to the winter hemisphere at 12 LT. Further, the higher electron density values in the summer EIA crest are maintained at relatively higher altitudes throughout the afternoon hours (12–18 LT). The observed interhemispheric asymmetry of EIA has been explained by Lin et al. (2007) and Tulasi Ram, Su, and Liu (2009) as being due to the interplay between the transequatorial neutral winds and the equatorial plasma fountain. During the solstices, the transequatorial neutral winds blow from the summer hemisphere to the winter hemisphere. This transequatorial neutral wind transports the plasma upward/equatorward in the summer hemisphere and downward/poleward in the winter hemisphere due to the finite inclination of magnetic field lines. During the morning hours when the equatorial plasma fountain is relatively weak, the transequatorial winds can transport the plasma from the summer hemisphere to the winter hemisphere causing stronger winter EIA crests as observed around 09 LT. During noontime, the field-aligned plasma transport due to winds is counteracted by the strong equatorial plasma fountain. In the summer hemisphere, the plasma transport due to neutral winds and the equatorial fountain are in opposite directions, which leads to the formation of the stronger EIA crest at relatively higher altitudes in the summer hemisphere where the loss due to recombination is less. On the other hand, the transport due to the interhemispheric wind and the equatorial fountain are in the same direction in the winter hemisphere. Thus, the transport due to wind and equatorial fountain acts together to push the plasma to lower altitudes where the recombination loss is larger, causing weaker EIA crest in the Southern Hemisphere. Similar interhemispheric asymmetry of EIA with stronger EIA crests at relatively higher altitudes in the summer (Southern) hemisphere than in the winter (Northern) hemisphere can also be observed during the December solstice (Figure 8c) around 09–21 LT. The temporal evolution of EIA and its interhemispheric asymmetries during the solstices observed in Figures 8b and 8c are consistent with previous reports by Lin et al. (2007), Tulasi Ram, Su, and Liu (2009), Balan et al. (2013), Luan et al. (2015), and Sai Gowtam and Tulasi Ram (2017c). It is interesting to note that the effects of the interaction between transequatorial neutral winds and the equatorial fountain process during solstices has been successfully captured by the ANNIM-3D. Another interesting observation from Figures 8b and 8c is that the ionization during the December solstice (Figure 8c) is significantly higher than in the June solstice (Figure 8b) at all local times, which is generally known as ionospheric annual anomaly (Berkner & Wells, 1938; Dang et al., 2017; Mendillo et al., 2005; Rishbeth & Muller-Wodarg, 2006; Sai Gowtam & Tulasi Ram, 2017b; Yonezawa, 1971; Zeng et al., 2008). Therefore, from Figures 8a to 8c, we can conclude that the model has successfully captured the diurnal evolution, the seasonal variations of EIA and its interhemispheric asymmetries during solstices, and the ionospheric annual anomaly.

Another interesting observation from Figure 8 is that the electron density values below the *F*2-peak altitudes are showing slightly higher values around the dip equator and relatively lower values below the anomaly crests as shown by magenta arrows in the panel that corresponds to 12 LT of Figure 8a. One can clearly see similar one peak and two caves structure below 200-km altitudes in other panels too during the hours when the EIA is well developed. A similar latitudinal variation of the electron density below the *F*2 peak was earlier reported in the FORMOSAT-3/COSMIC RO observations by Liu et al. (2010) and Yue et al. (2010) and referred to as the "artificial plasma caves." This latitudinal structure is mainly due to the inherent and systematic bias that is introduced in the standard Abel retrieval of electron density profiles from GPS-RO measurements under the assumption of spherical symmetry (Hajj et al., 2000; Hajj & Romans, 1998). However, the spherical symmetry assumption is poorly valid around the EIA latitudes, which leads to the formation of pseudo troughs (caves) below the EIA crests at low latitudes and a pseudo peak below the EIA trough at equatorial latitudes (Liu et al., 2010; Tulasi Ram et al., 2016; Yue et al., 2010). It seems that the ANNIM-3D has captured this feature as the model is heavily weighted by the GPS-RO data. Nonetheless, it also indicates that the present ANN architecture and the training method adopted in the development of ANNIM-3D has successfully captured this feature that is inherently present in the GPS-RO data.

4.5. Main Ionospheric Trough

The latitudinal distribution of electron density often exhibits a large-scale plasma depletion at subauroral latitudes, known as the main ionospheric trough. With a view of examining this feature with the ANNIM-3D, the latitudinal-altitudinal variation of electron density (longitudinal cut) along the Indian (75°E)

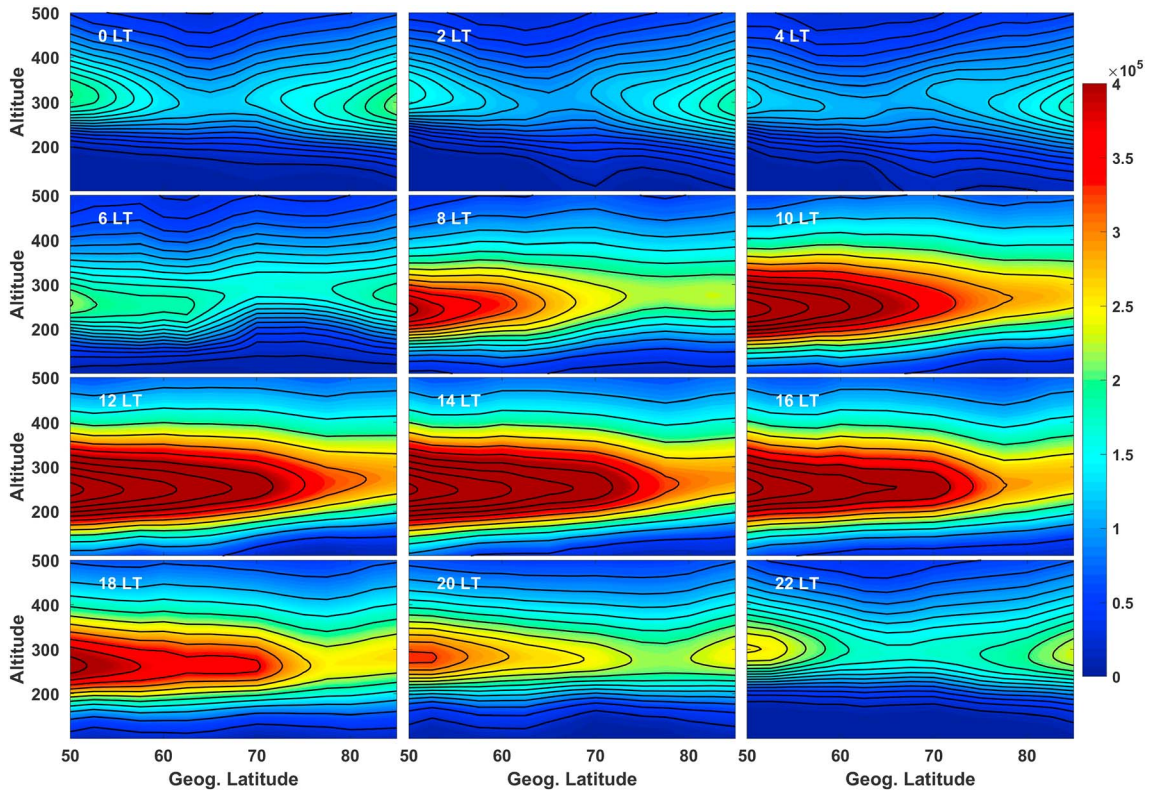

Figure 9. The latitudinal and altitudinal distribution of electron density simulated using artificial neural network-based global three-dimensional ionospheric model along Indian (75°E) sector during the March equinox showing the main ionospheric trough at nighttimes.

sector is shown for different local times in Figure 9. Figure 9 is constructed from the model run used for Figure 8a; however, it focuses on 50° to 87.5°N latitudes with enhanced color scale for better visibility of the main ionospheric trough features. A depletion in electron density between middle and high latitudes can be observed from this figure particularly during nighttime. A small trough appears around 78°N at 18 LT that becomes clearer and strengthens as the night progresses. Further, the location of the trough moves equatorward and reaches ~65°N around 02-04 LT. The trough weakens and moves poleward after sunrise (06–08 LT) and disappears completely by 10 LT. The observed local time variations in the location and strength of the trough are consistent with the main ionospheric trough between the middle and high latitudes reported in the literature (Lee et al., 2011; Moffett & Quegan, 1983 and Parker et al., 2018).

4.6. Ionospheric Response Under Quiet and Disturbed Geomagnetic Conditions

In order to study the ANNIM-3D response for quiet and disturbed geomagnetic activity conditions, we have run the model for two cases with $Kp = 2$ (quiet) and $Kp = 8$ (disturbed) while keeping all the other inputs unchanged. Figure 10 presents the longitudinal and latitudinal distributions of N_mF2 (left panels) and h_mF2 (right panels) at global local noon (12 LT) for day number 80 under moderate solar activity conditions ($F10.7 = 120$ sfu). The top (Figures 10a and 10b) and middle (Figures 10c and 10d) panels correspond to quiet ($Kp = 2$) and disturbed ($Kp = 8$) geomagnetic activity conditions, respectively. The bottom panels (Figures 10e and 10f) represent the relative deviations in N_mF2 and h_mF2 (ΔN_mF2 and Δh_mF2) predicted by ANNIM-3D for disturbed conditions with respect to quiet conditions and expressed in percentage. From Figure 10e, one can observe that the ΔN_mF2 is largely negative (40% to 50%) indicating a negative ionospheric storm at middle and high latitudes (>~45°) in both the hemispheres. On the other hand, the ΔN_mF2 exhibits small positive values (5% to 15%) indicating a positive ionospheric storm at equatorial and low-latitude region. The Δh_mF2 variations presented in Figure 10f show a significant enhancement (about 20% to 30%) around the auroral and high-latitude regions but only a small positive values at low and middle latitudes.

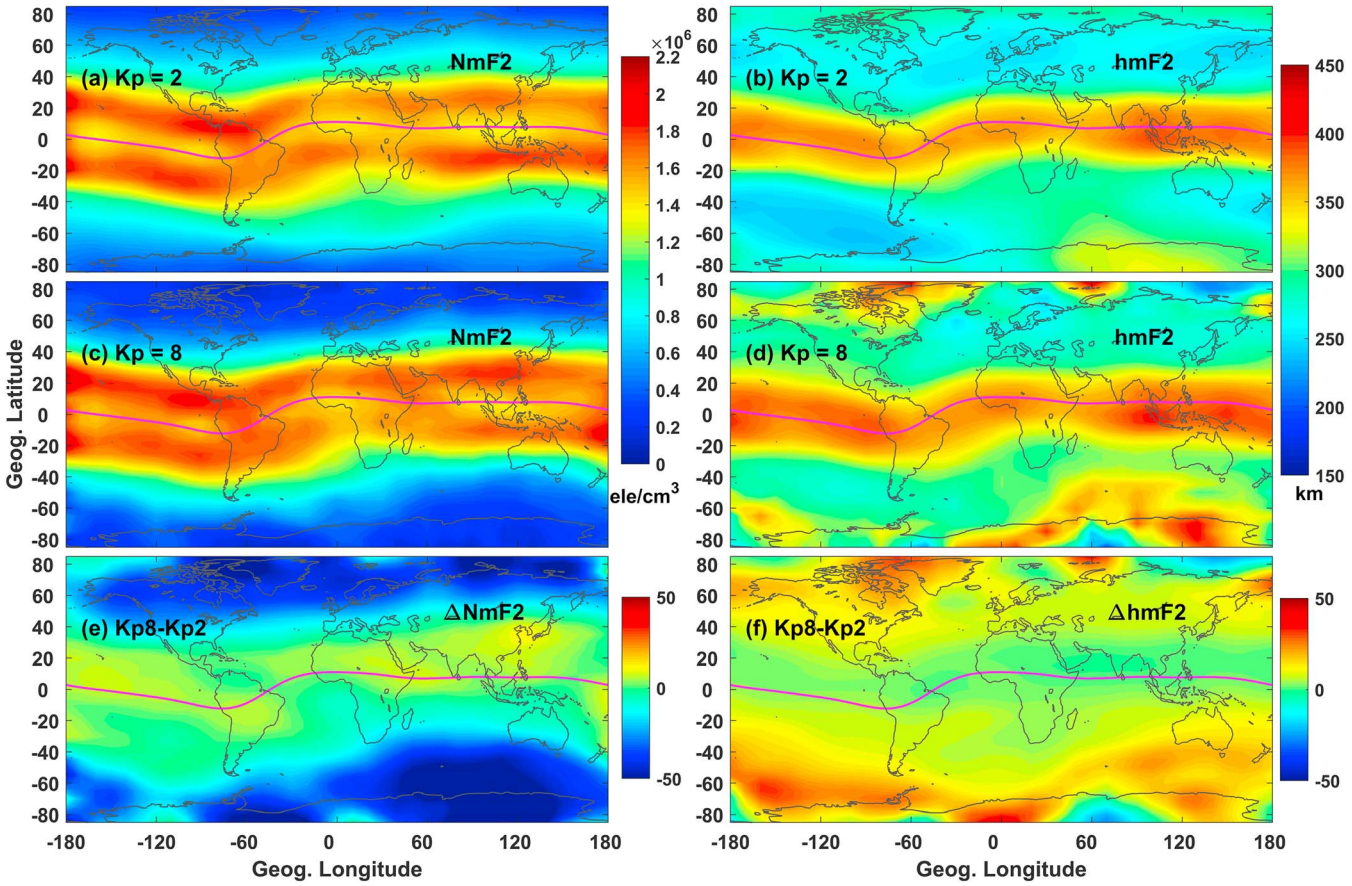

Figure 10. Spatial (geographic longitude and latitude) distributions of N_mF2 (left panels) and h_mF2 (right panels) simulated using artificial neural network-based global three-dimensional ionospheric model under quiet ($Kp = 2$) and disturbed ($Kp = 9$) geomagnetic conditions. Figures 10e and 10f (bottom panels) present the disturbances in N_mF2 and h_mF2, respectively, under disturbed ($Kp = 8$) conditions with respect to quiet-time ($Kp = 2$) conditions expressed in percentage.

During the geomagnetically disturbed periods, the enhanced particle and Joule heating at auroral latitudes leads to strong meridional wind circulation (Fuller-Rowell et al., 1994). The upwelling neutral wind at auroral and high latitudes causes significant changes in the thermospheric neutral composition and O/N_2 density ratio decreases because of upwelling molecular rich air. As a result, the plasma density decreases due to increased recombination loss with neutrals causing a negative ionospheric storm at high and middle latitudes. The equatorward boundary of negative ionospheric storm disturbance can vary depending on the strength of meridional wind circulation cells, which in turn depend on the geomagnetic activity and auroral precipitation. The meridional wind circulation brings the atomic oxygen-rich air to low latitudes and the ionospheric plasma density increases causing a positive ionospheric storm (Crowley et al., 2008; Strickland et al., 2001). Hence, the negative ionospheric storm predicted by ANNIM-3D for high and middle latitudes and positive ionospheric storm for low latitudes (Figure 10e) are consistent with the storm-time meridional wind circulation and associated neutral composition changes (Fuller-Rowell et al., 1994; Crowley et al., 2008; Pedatella et al., 2010 and Tulasi Ram, Lei, et al., 2010, Tulasi Ram, Liu, et al., 2010). The Joule and particle heating at high latitudes further causes the thermal expansion of upper atmosphere and increased neutral and plasma scale heights (Lei et al., 2008; Sojka et al., 2009; Thayer et al., 2008). The significantly enhanced Δh_mF2 (~20–30%) at auroral and high latitudes (Figure 10f) can be attributed to thermal expansion due to particle and Joule heating during the enhanced geomagnetic activity periods. Therefore, from the results presented in Figure 10, one can conclude that the storm-time ionospheric changes predicted by the ANNIM-3D are consistent with the particle precipitation, Joule heating, and meridional wind circulation mechanisms reported in the literature.

It should be mentioned here that the present model considers the *Kp* index to represent the geomagnetic disturbances; however, the *Kp* index does not indicate the phase of a geomagnetic storm. On the other hand, the ionospheric response during the geomagnetic storm periods depends highly on upstream solar wind conditions and phase of the storm through different electrodynamic disturbances, composition changes and neutral wind circulations. The present ANNIM-3D with *Kp* index input can only represent the ionospheric disturbances due to composition changes associated meridional wind circulation. Certainly, this model needs thorough validations and further improvements for disturbed space weather periods.

5. Summary, Limitations, and Future Improvements

A new global three-dimensional ionospheric model, namely, ANNIM-3D, has been developed using the long-term ionospheric observations from global Digisonde, topside sounder, and GPS-RO measurements by implementing the ANNs. The ANNIM-3D model predictions have been thoroughly validated with ground-based Digisonde (Figure 4), ISRs (Figure 5), and satellite in situ observations at different altitudes (Figures 6 and 7) alongside the well-established empirical model IRI 2016. In general, the ANNIM-3D results are found to be consistent with the ground-based and satellite in situ observations. Further, the ANNIM-3D better represents the topside in situ electron density observations by ROCSAT-1 and SWARM-A than the IRI 2016 model (Figure 6) with higher regression coefficients and smaller RMS errors (Figure 7). However, the ANNIM-3D slightly underestimates the electron density when compared with the in situ observations of CHAMP (at 385 km) near the *F*2-peak altitudes. The ANNIM-3D has also successfully reproduced the diurnal evolution, seasonal variations of EIA and its interhemispheric asymmetries during solstices (Figure 8). Further, the large-scale ionospheric features such as ionospheric annual anomaly and main ionospheric trough are well represented by this model (Figures 8 and 9). Moreover, the new model also successfully predicted the ionospheric changes due to neutral composition changes associated with high-latitude heating and meridional wind circulation during disturbed geomagnetic activity periods (Figure 10).

The observational data assimilated in this model come from the descending phase of solar cycle 23 and solar cycle 24. Nevertheless, the vertical electron density profiles simulated from ANNIM-3D under varying *F*10.7 solar flux conditions and comparison with Digisonde observations (Figure 4) indicate that the new model is valid over the solar flux values ranging from 60 to 220 sfu. The low to moderate solar activity pertinence of data assimilated in this model could impact the model prediction for very high solar flux conditions (e.g., $F10.7 > 220$ sfu). This shortcoming will be overcome when additional data, particularly from the high solar activity periods, are included in the model development.

It may also be recalled here that this model initially predicts the vertical electron density profile between 150 and 700 km and then extrapolates up to 1,000 km using α-Chapman function (equation (1)) and down to 70 km using IRI function (equation (2)). These profile extrapolations may also introduce some error in the predicted electron densities, particularly, in the bottomside where the same IRI function (equation (2)) is employed to extrapolate the profile between the altitudes from 150 to 70 km (which include the *F*1, *E*, and *D* regions during daytime). In other words, the present version of this model cannot properly treat the *F*1 and *E* layers, a limitation that will be addressed in future efforts. The extrapolation of the bottomside profile between 150 and 70 km could also be one of the reasons for the consistent overestimation of the bottomside density compared with Millstone Hill ISR observations (Figure 5b); however, such a consistent overestimation is not observed at Jicamarca (Figure 5a).

Further, the spherical uniformity of electron density is one of the major assumptions in the retrieval of vertical electron density profiles from GPS-RO observations (Yue et al., 2010). However, this assumption is often violated at the EIA latitudes where the horizontal density gradients are larger. Hence, the *F*2-layer peak density is often underestimated around the EIA crest latitudes, whereas the electron densities around the dip equator are slightly overestimated in GPS-RO data. Since the present model is largely based on the GPS-RO data, the systematic errors introduced in the Abel retrieval are also captured by ANNIM-3D. This can be seen the artificial plasma caves at altitudes below 200 km in the latitude-altitude-electron density distributions presented in Figure 8. This could also be one of the reasons for the slightly underestimated electron density values predicted by the ANNIM-3D compared to the CHAMP in situ observations around 385-km altitude. Tulasi Ram et al. (2016) have developed a self-consistent improved Abel retrieval method by incorporating suitable weights that can account for the spherical inhomogeneity while retrieving the electron

density profiles in GPS-RO observations. Assimilation of corrected and improved GPS-RO data using the Tulasi Ram et al. (2016) method may reduce the errors associated with GPS-RO, which will be addressed in our future efforts.

Finally, the present model can also predict the ionospheric disturbances due to disturbed geomagnetic conditions that are consistent with Joule heating and meridional wind circulation. However, the present model considers only *Kp* index, which cannot distinguish between the different phases of the geomagnetic storm and upstream solar wind conditions. Assimilation of suitable electric field models and high-latitude energy inputs would improve the model performance, which will be addressed in our continued efforts to improve this model for varying space weather conditions.

Acknowledgments
This work was supported by SERB, DST, Government of India through project ECR-2017-002271. The Formosat-3/COSMIC, CHAMP, and GRACE RO data are obtained from UCAR-CDAAC (http://cdaac-www.cosmic.ucar.edu/cdaac/products.html). We sincerely acknowledge the GIRO data providers for making the Digisonde data available through GIRO-DIDBase (http://giro.uml.edu/didbase/scaled.php). The true height profile data from the ISIS topside sounders have been obtained from GSFC Space Physics Data Facility (ftp://spdf.gsfc.nasa.gov/pub/data/isis/topside_sounder/). We sincerely acknowledge the open data policy of ROCSAT-1 (http://140.115.111.70/IPEI_DataSet/dataset_title.html), SWARM-A (https://swarm-diss.eo.esa.int/#) and CHAMP (http://isdc-old.gfz-potsdam.de/) mission data. The incoherent scatter radars data are obtained from the Madrigal Database at Cornell (http://landau.geo.cornell.edu/madrigal/index.html/). The ANN training and model computations were carried out using the High Performance Computing System at the Indian Institute of Geomagnetism.

References

Altadill, D., Magdaleno, S., Torta, M. J., & Blanch, E. (2013). Global empirical models of the density peak height and of the equivalent scale height for quiet conditions. *Advances in Space Research*, *52*(10), 1756–1769. https://doi.org/10.1016/j.asr.2012.11.018

Athieno, R., Jayachandran, P. T., & Themens, D. R. (2017). A neural network-based foF2 model for a single station in the polar cap. *Radio Science*, *52*, 784–796. https://doi.org/10.1002/2016RS006192

Bailey, G. J., & Balan, N. (1996). A low-latitude ionosphere-plasmasphere model. In R. W. Schunk (Ed.), *STEP handbook on ionospheric models* (pp. 173–206). Logan: Utah State University.

Bailey, G. J., Balan, N., & Su, Y. Z. (1997). The Sheffield University plasmasphere-ionosphere model—A review. *Journal of Atmospheric and Solar - Terrestrial Physics*, *59*(13), 1541–1552. https://doi.org/10.1016/S1364-6826(96)00155-1

Balan, N., Rajesh, P. K., Sripathi, S., Tulasi Ram, S., Liu, J. Y., & Bailey, G. J. (2013). Modeling and observations of the north–south ionospheric asymmetry at low latitudes at long deep solar minimum. *Space Research*, *53*(5), 724–733. https://doi.org/10.1016/j.asr.2013.12.019

Benson, R. F. (2010). Four decades of space-borne radio sounding. *Radio Science Bulletin*, *333*, 24–44.

Berkner, L. V., & Wells, H. W. (1938). Non-seasonal change of F_2-region ion density. *Terrestrial Magnetism and Atmospheric Electricity*, *43*(1), 15–36. https://doi.org/10.1029/TE043i001p00015

Bilitza, D. (2001). International Reference Ionosphere. *Radio Science*, *36*(2), 261–275.

Bilitza, D., Altadill, D., Truhlik, V., Shubin, V., Galkin, I., Reinisch, B., & Huang, X. (2017). International Reference Ionosphere 2016: From ionospheric climate to real-time weather predictions. *Space Weather*, *15*, 418–429. https://doi.org/10.1002/2016SW001593

Bilitza, D., Altadill, D., Zhang, Y., Mertens, C., Truhlik, V., Richards, P., et al. (2014). The International Reference Ionosphere 2012—A model of international collaboration. *Journal of Space Weather and Space Climate*, *4*, 1–12. https://doi.org/10.1051/swsc/2014004

Bilitza, D., Huang, X., Reinisch, B. W., Benson, R. F., Hills, H. K., & Schar, W. B. (2004). Topside Ionogram Scaler With True Height Algorithm (TOPIST): Automated processing of ISIS topside ionograms. *Radio Science*, *39*, RS1S27. https://doi.org/10.1029/2002RS002840

Bilitza, D., & Reinisch, B. W. (2008). International Reference Ionosphere 2007: Improvements and new parameters. *Advances in Space Research*, *42*(4), 599–609. https://doi.org/10.1016/j.asr.2007.07.048

Bilitza, D., Reinisch, B. W., Radicella, S. M., Pulinets, S., Gulyaeva, T., & Triskova, L. (2006). Improvements of the International Reference Ionosphere model for the topside electron density profile. *Radio Science*, *41*, RS5S15. https://doi.org/10.1029/2005RS003370

Booker, H. G. (1977). Fitting of multi-region ionospheric profiles of electron density by a single analytic function of height. *Journal of Atmospheric and Terrestrial Physics*, *39*(5), 619–623. https://doi.org/10.1016/0021-9169(77)90072-1

Chapman, S. (1931a). The absorption and dissociative or ionizing effect of monochromatic radiation in an atmosphere on a rotating earth. *Proceedings of the Physical Society of London*, *45*, 26–45.

Chapman, S. (1931b). The absorption and dissociative or ionizing effect of monochromatic radiation in an atmosphere on a rotating earth. *Proceedings of the Physical Society of London*, *43*, 433–501.

Clausen, L. B. N., & Nickisch, H. (2018). Automatic classification of auroral images from the Oslo Auroral THEMIS (OATH) data set using machine learning. *Journal of Geophysical Research: Space Physics*, *123*, 5640–5647. https://doi.org/10.1029/2018JA025274

Crowley, G., Reynolds, A., Thayer, J. P., Lei, J., Paxton, L. J., Christensen, A. B., et al. (2008). Periodic modulations in thermospheric composition by solar wind high speed streams. *Geophysical Research Letters*, *35*, L21106. https://doi.org/10.1029/2008GL035745

Dang, T., Wang, W., Burns, A., Dou, X., Wan, W., & Lei, J. (2017). Simulations of the ionospheric annual asymmetry: Sun-Earth distance effect. *Journal of Geophysical Research: Space Physics*, *122*, 6727–6736. https://doi.org/10.1002/2017JA024188

Di Giovanni, G., & Radicella, S. M. (1990). An analytical model of the electron density profile in the ionosphere. *Advances in Space Research*, *10*(11), 27–30. https://doi.org/10.1016/0273-1177(90)90301-F

Drob, D. P., Emmert, J. T., Meriwether, J. W., Makela, J. J., Doornbos, E., Conde, M., & Klenzing, J. H. (2015). An update to the horizontal wind model (HWM): The quiet time thermosphere. *Earth and Space Science*, *2*, 301–319. https://doi.org/10.1002/2014EA000089

Fuller-Rowell, T. J., Codrescu, M. V., Moffett, R. J., & Quegan, S. (1994). Response of the thermosphere and ionosphere to geomagnetic storms. *Journal of Geophysical Research*, *99*(A3), 3893–3914. https://doi.org/10.1029/93JA02015

Fuller-Rowell, T. J., Rees, D., Quegan, S., Moffett, R. J., Codrescu, M. V., & Millward, G. H. (1996). A coupled thermosphere-ionosphere model (CTIM). In R. W. Schunk (Ed.), *STEP: Handbook of ionospheric models* (pp. 217–238). Logan, Utah: Utah State University.

Galkin, I. A., Khmyrov, G. M., Kozlov, A. V., Reinisch, B. W., Huang, X., & Paznukhov, V. V. (2008). The ARTIST 5, in Radio sounding and plasma physics. *AIP Conf. Proc.*, *974*, 150–159. https://doi.org/10.1063/1.2885024

Hagan, M. T., & Menhaj, M. (1994). Training multilayer networks with the Marquardt algorithm. *IEEE Transactions on Neural Networks*, *5*(6), 989–993.

Hajj, G., Lee, L., Pi, X., Romans, L., Schreiner, W., Straus, P., & Wang, C. (2000). COSMIC GPS ionospheric sensing and space weather. *Terrestrial, Atmospheric and Oceanic Sciences*, *11*(1), 235–272. https://doi.org/10.3319/TAO.2000.11.1.235(COSMIC)

Hajj, G. A., & Romans, L. J. (1998). Ionospheric electron density profiles obtained with the global positioning system: Results from the GPS/MET experiment. *Radio Science*, *33*(1), 175–190. https://doi.org/10.1029/97RS03183

Hargreaves, J. K. (1979). *The upper atmosphere and solar-terrestrial relations: An introduction to the aerospace environment* (pp. 1–298). New York: Van Nostrand Reinhold.

Hargreaves, J. K. (1992). *The solar-terrestrial environment* (pp. 1–420). New York: Cambridge University Press. https://doi.org/10.1017/CBO9780511628924

Hochegger, G., Nava, B., Radicella, S. M., & Leitinger, R. (2000). A family of ionospheric models for different uses. *Physics and Chemistry of the Earth, Part C: Solar, Terrestrial & Planetary Science*, *25*(4), 307–310.

Hu, A., & Zhang, K. (2018). Using bidirectional long short-term memory method for the height of F2 peak forecasting from ionosonde measurements in the Australian region. *Remote Sensing*, *10*(10), 1658. https://doi.org/10.3390/rs10101658

Huang, X., Reinisch, B. W., Bilitza, D., & Benson, R. F. (2002). Electron density profiles of the topside ionosphere. *Annali di Geofisica*, *45*, 125–130.

Huang, Z., & Yuan, H. (2014). Ionospheric single-station TEC short-term forecast using RBF neural network. *Radio Science*, *49*, 283–292. https://doi.org/10.1002/2013RS005247

Huba, J. D., Joyce, G., & Fedder, J. A. (2000). Sami2 is another model of the ionosphere (SAMI2): A new low-latitude ionosphere model. *Journal of Geophysical Research*, *105*(A10), 23035–23053. https://doi.org/10.1029/2000JA000035

Huba, J. D., Joyce, G., & Krall, J. (2008). Three-dimensional equatorial spread F modeling. *Geophysical Research Letters*, *35*, L10102. https://doi.org/10.1029/2008GL033509

Hysell, D. L. (2000). Incoherent scatter experiments at Jicamarca using alternating codes. *Radio Science*, *35*, 1425.

Hysell, D. L., Rodrigues, F. S., Chau, J. L., & Huba, J. D. (2008). Full profile incoherent scatter analysis at Jicamarca. *Annales Geophysicae*, *26*(1), 59–75. https://doi.org/10.5194/angeo-26-59-2008

Kumluca, A., Tulunay, E., Topalli, I., & Tulunay, Y. (1999). Temporal and spatial forecasting of ionospheric critical frequency using neural networks. *Radio Science*, *34*(6), 1497–1506. https://doi.org/10.1029/1999RS900070

Lamming, X., & Cander, L. R. (1999). Monthly median foF2 modelling COST 251 area by neural networks. *Physics and Chemistry of the Earth - Part C*, *24*, 349–354.

Lee, I. T., Wang, W., Liu, J. Y., Chen, C. Y., & Lin, C. H. (2011). The ionospheric midlatitude trough observed by FORMOSAT-3/COSMIC during solar minimum. *Journal of Geophysical Research*, *116*, A06311. https://doi.org/10.1029/2010JA015544

Lei, J., Thayer, J. P., Forbes, J. M., Sutton, E. K., & Nerem, R. S. (2008). Rotating solar coronal holes and periodic modulation of the upper atmosphere. *Geophysical Research Letters*, *35*, L10109. https://doi.org/10.1029/2008GL033875

Lei, J., Syndergaard, S., & Burns, A. G. (2007). Comparison of COSMIC ionospheric measurements with ground-based observations and model predictions: Preliminary results. *Journal of Geophysical Research*, *112*, A07308. https://doi.org/10.1029/2006JA012240

Levenberg, K. (1944). A method for the solution of certain non-linear problems in least squares. *Quarterly of Applied Mathematics*, *2*(2), 164–168. https://doi.org/10.1090/qam/10666

Lin, C. H., Liu, J. Y., Fang, T. W., Chang, P. Y., Tsai, H. F., Chen, C. H., & Hsiao, C. C. (2007). Motions of the equatorial ionization anomaly crests imaged by FORMOSAT-3/COSMIC. *Geophysical Research Letters*, *34*, L19101. https://doi.org/10.1029/2007GL030741

Liu, J. Y., Lin, C. Y., Lin, C. H., Tsai, H. F., Solomon, S. C., Sun, Y. Y., et al. (2010). Artificial plasma cave in the low-latitude ionosphere results from the radio occultation inversion of the FORMOSAT-3/COSMIC. *Journal of Geophysical Research*, *115*, A07319. https://doi.org/10.1029/2009JA015079

Luan, X., Wang, P., Dou, X. K., & Liu, Y. C.-M. (2015). Interhemispheric asymmetry of the equatorial ionization anomaly in solstices observed by COSMIC during 2007–2012. *Journal of Geophysical Research: Space Physics*, *120*, 3059–3073. https://doi.org/10.1002/2014JA020820

Marquardt, D. W. (1963). An algorithm for the least-squares estimation of nonlinear parameters. *SIAM Journal of Applied Mathematics*, *11*(2), 431–441. https://doi.org/10.1137/0111030

Mendillo, M., Huang, C.-L., Pi, X., Rishbeth, H., & Meier, R. (2005). The global ionospheric asymmetry in total electron content. *Journal of Atmospheric and Solar - Terrestrial Physics*, *67*(15), 1377–1387. https://doi.org/10.1016/j.jastp.2005.06.021

Moffett, R. J., & Quegan, S. (1983). The midlatitude trough in the electron concentration of the ionospheric F layer: A review of observations and modelling. *Journal of Atmospheric and Terrestrial Physics*, *45*(5), 315–343. https://doi.org/10.1016/S0021-9169(83)80038-5

Nava, B., Radicella, S. M., Leitinger, R., & Coisson, P. (2006). A near-real-time model-assisted ionosphere electron density retrieval method. *Radio Science*, *41*, RS6S16. https://doi.org/10.1029/2005RS003386

Oyeyemi, E. O., & Poole, A. W. V. (2004). Towards the development of a new global foF2 empirical model using neural networks. *Advances in Space Research*, *34*(9), 1966–1972. https://doi.org/10.1016/j.asr.2004.06.010

Oyeyemi, E. O., Poole, A. W. V., & McKinnell, L. A. (2005). On the global model for foF2 using neural networks. *Radio Science*, *40*, RS6011. https://doi.org/10.1029/2004RS003223

Parker, J. A. D., Pryse, S. E., Jackson-Booth, N., & Buckland, A. (2018). Modelling the main ionospheric trough using the Electron Density Assimilative Model (EDAM) with assimilated GPS TEC. *Annales de Geophysique*, *36*(1), 125–138. https://doi.org/10.5194/angeo-36-125-2018

Pedatella, N. M., Lei, J., Thayer, J. P., & Forbes, J. M. (2010). Ionosphere response to recurrent geomagnetic activity: Local time dependency. *Journal of Geophysical Research*, *115*, A02301. https://doi.org/10.1029/2009JA014712

Poole, A. W. V., & Poole, M. (2002). Long-term trends in foF2 over Grahamstown using neural networks. *Annals of Geophysics*, *45*, 155–161.

Potula, B. S., Chu, Y.-H., Uma, G., Hsia, H.-P., & Wu, K.-H. (2011). A global comparative study on the ionospheric measurements between COSMIC radio occultation technique and IRI model. *Journal of Geophysical Research*, *116*, A02310. https://doi.org/10.1029/2010JA015814

Radicella, S. M., & Leitinger, R. (2001). The evolution of the DGR approach to model electron density profiles. *Advances in Space Research*, *27*(1), 35–40. https://doi.org/10.1016/S0273-1177(00)00138-1

Rawer, K. (1988). Synthesis of ionospheric electron density profiles with Epstein functions. *Advances in Space Research*, *8*(4), 191–199. https://doi.org/10.1016/0273-177(88)90239-6

Rawer, K., Bilitza, D., & Gulyaeva, T. L. (1985). New formulas for IRI electron density profile in the topside and middle ionosphere. *Advances in Space Research*, *5*(7), 3–12. https://doi.org/10.1016/0273-1177(85)90347-3

Reinisch, B. W., & Galkin, I. A. (2011). Global Ionospheric Radio Observatory (GIRO). *Earth, Planets and Space*, *63*(4), 377–381. https://doi.org/10.5047/eps.2011.03.001

Reinisch, B. W., Galkin, I. A., Khmyrov, G. M., Kozlov, A. V., Bibl, K., Lisysyan, I. A., et al. (2009). The new Digisonde for research and monitoring applications. *Radio Science*, *44*, RS0A24. https://doi.org/10.1029/2008RS004115

Reinisch, B. W., & Huang, X. (2001). Deducing topside profiles and total electron content from bottomside ionograms. *Advances in Space Research*, *27*(1), 23–30. https://doi.org/10.1016/S0273-1177(00)0013608

Reinisch, B. W., Huang, X., Belehaki, A., Shi, J., Zhang, M., & Ilma, R. (2004). Modeling the IRI topside profile using scale height from ground based ionosonde measurements. *Advances in Space Research*, *34*(9), 2026–2031. https://doi.org/10.1016/j.asr.2004.06.012

Reinisch, B. W., Nsumei, P., Huang, X., & Bilitza, D. K. (2007). Modeling the F2 topside and plasma sphere for IRI using IMAGE/RPI and ISIS data. *Advances in Space Research*, *39*(5), 731–738. https://doi.org/10.1016/j.asr.2006.05.032

Richmond, A. D., Ridley, E. C., & Roble, R. G. (1992). A thermosphere/ionosphere general circulation model with coupled electrodynamics. *Geophysical Research Letters*, *19*(6), 601–604. https://doi.org/10.1029/92GL00401

Rishbeth, H., & Muller-Wodarg, I. C. F. (2006). Why is there more ionosphere in January than in July? The annual asymmetry in the F2-layer. *Annales de Geophysique*, *24*(12), 3293–3311. https://doi.org/10.5194/angeo-24-3293-2006

Rius, A., Ruffini, G., & Romeo, A. (1998). Analysis of ionospheric electron-density distribution from GPS/MET occultations. *IEEE Transactions on Geoscience and Remote Sensing*, *36*(2), 383–394. https://doi.org/10.1109/36.662724

Roble, R. G., Ridley, E. C., Richmond, A. D., & Dickinson, R. E. (1988). A coupled thermosphere/ionosphere general circulation model. *Geophysical Research Letters*, *15*(12), 1325–1328. https://doi.org/10.1029/GL015i012p01325

Rumelhart, D. E., Hinton, G. E., & Williams, R. (1986). Learning representations by back-propagating errors. *Nature*, *323*(6088), 533–536. https://doi.org/10.1038/323533a0

Sai Gowtam, V., & Tulasi Ram, S. (2017a). An artificial neural network based ionospheric model to predict N_mF_2 and h_mF_2 using long-term data set of FORMOSAT-3/COSMIC radio occultation observations: Preliminary results. *Journal of Geophysical Research: Space Physics*, *122*, 11,743–11,755. https://doi.org/10.1002/2017JA024795

Sai Gowtam, V., & Tulasi Ram, S. (2017b). Ionospheric annual anomaly—New insights to the physical mechanisms. *Journal of Geophysical Research: Space Physics*, *122*, 8816–8830. https://doi.org/10.1002/2017JA024170

Sai Gowtam, V., & Tulasi Ram, S. (2017c). Ionospheric winter anomaly and annual anomaly observed from Formosat-3/COSMIC radio occultation observations during the ascending phase of solar cycle 24. *Advances in Space Research*, *60*(8), 1585–1593. https://doi.org/10.1016/j.asr.2017.03.017

Schreiner, W. S., Rocken, C., Sokolovskiy, S., Syndergaard, S., & Hunt, D. C. (2007). Estimates of the precision of GPS radio occultation from the COSMIC/FORMOSAT-3 mission. *Geophysical Research Letters*, *34*, L04808. https://doi.org/10.1029/2006GL027557

Schreiner, W. S., Sokolovsky, S. V., & Rocken, C. (1999). Analysis and validation of GPS/MET radio occultation data in the ionosphere. *Radio Science*, *34*(4), 949–966. https://doi.org/10.1029/1999RS900034

Shubin, V. N. (2017). Global empirical model of critical frequency of the ionospheric F2-layer for quiet geomagnetic conditions, 2017. *Geomagnetism and Aeronomy*, *57*(4), 414–425. https://doi.org/10.1134/S0016793217040181

Sojka, J. J., Nicolls, M. J., Heinselman, C. J., & Kelly, J. D. (2009). The PFISR IPY observations of ionospheric climate and weather. *Journal of Atmospheric and Solar-Terrestrial Physics*, *71*, 771–785. https://doi.org/10.1016/j.jastp.2009.01.001

Stankov, S. M., Jakowski, N., Heise, S., Muhtarov, P., Kutiev, I., & Warnant, R. (2003). A new method for reconstruction of the vertical electron density distribution in the upper ionosphere and plasmasphere. *Journal of Geophysical Research*, *108*(A5), 1164. https://doi.org/10.1029/2002JA009570

Strickland, D. J., Daniell, R. E., & Craven, J. D. (2001). Negative ionospheric storm coincident with DE 1-observed thermospheric disturbance on October 14, 1981. *Journal of Geophysical Research*, *106*(A10), 21,049–21,062. https://doi.org/10.1029/2000JA000209

Syndergaard, S., Schreiner, W. S., Rocken, C., Hunt, D. C., & Dymond, K. F. (2006). Preparing for COSMIC: Inversion and analysis of ionospheric data products. In U. Foelsche, G. Kirchengast, & A. K. Steiner (Eds.), *Atmosphere and climate: Studies by occultation methods* (pp. 137–146). Berlin: Springer. https://doi.org/10.1007/3-540-34121-8_12

Thayer, J. P., Lei, J., Forbes, J. M., Sutton, E. K., & Nerem, R. S. (2008). Thermospheric density oscillations due to periodic solar wind high-speed streams. *Journal of Geophysical Research*, *113*, A06307. https://doi.org/10.1029/2008JA013190

Thébault, E., Finlay, C. C., Beggan, C. D., Alken, P., Aubert, J., Barrois, O., et al. (2015). International geomagnetic reference field: The 12th generation. *Earth, Planets and Space*, *67*(1), 79. https://doi.org/10.1186/s40623-015-0228-9

Themens, D. R., Jayachandran, P. T., Galkin, I., & Hall, C. (2017). The Empirical Canadian High Arctic Ionospheric Model (E-CHAIM): N_mF_2 and h_mF_2. *Journal of Geophysical Research: Space Physics*, *122*, 9015–9031. https://doi.org/10.1002/2017JA024398

Tulasi Ram, S., Lei, J., Su, S.-Y., Liu, C. H., Lin, C. H., & Chen, W. S. (2010). Dayside ionospheric response to recurrent geomagnetic activity during the extreme solar minimum of 2008. *Geophysical Research Letters*, *37*, L02101. https://doi.org/10.1029/2009GL041038

Tulasi Ram, S., Liu, C. H., & Su, S.-Y. (2010). Periodic solar wind forcing due to recurrent coronal holes during 1996–2009 and its impact on Earth's geomagnetic and ionospheric properties during the extreme solar minimum. *Journal of Geophysical Research*, *115*, A12340. https://doi.org/10.1029/2010JA015800

Tulasi Ram, S., Sai Gowtam, V., Mitra, A., & Reinisch, B. (2018). The improved two-dimensional artificial neural network-based ionospheric model (ANNIM). *Journal of Geophysical Research: Space Physics*, *123*, 5807–5820. https://doi.org/10.1029/2018JA025559

Tulasi Ram, S., Su, S.-Y., & Liu, C. H. (2009). FORMOSAT-3/COSMIC observations of seasonal and longitudinal variations of equatorial ionization anomaly and its interhemispheric asymmetry during the solar minimum period. *Journal of Geophysical Research*, *114*, A06311. https://doi.org/10.1029/2008JA013880

Tulasi Ram, S., Su, S.-Y., Liu, C. H., Reinisch, B. W., & McKinnell, L.-A. (2009). Topside ionospheric effective scale heights (HT) derived with ROCSAT-1 and ground-based ionosonde observations at equatorial and midlatitude stations. *Journal of Geophysical Research*, *114*, A10309. https://doi.org/10.1029/2009JA014485

Tulasi Ram, S., Su, S.-Y., Tsai, L.-C., & Liu, C. H. (2016). A self-contained GIM-aided Abel retrieval method to improve GNSS-radio occultation retrieved electron density profiles. *GPS Solutions*, *20*(4), 825–836. https://doi.org/10.1007/s10291-015-0491-z

Uma, G., Brahmanandam, P. S., & Chu, Y. H. (2016). A long-term study on the deletion criterion of questionable electron density profiles caused by ionospheric irregularities–COSMIC radio occultation technique. *Advances in Space Research*, *57*(12), 2452–2463. https://doi.org/10.1016/j.asr.2016.03.034

Watthanasangmechai, K., Supnithi, P., Lerkvaranyu, S., Tsugawa, T., Nagatsuma, T., & Maruyama, T. (2012). TEC prediction with neural network for equatorial latitude station in Thailand. *Earth, Planets and Space*, *64*(6), 473–483. https://doi.org/10.5047/eps.2011.05.025

Wintoft, P. (2000). Twenty-four hour predictions of foF2 using neural networks. *Radio Science*, *35*, 395–408.

Xenos, T. D. (2002). Neural-network-based prediction techniques for single station modelling and regional mapping of the foF2 M(3000)F2 ionospheric characteristics. *Nonlinear Processes in Geophysics*, *9*(5/6), 477–486. https://doi.org/10.5194/npg-9-477-2002

Yang, K. F., Chu, Y. H., Su, C. L., Ko, H. T., & Wang, C. Y. (2009). An examination of FORMOSAT-3/COSMIC ionospheric electron density profile: Data quality criteria and comparisons with the IRI model. *Terrestrial, Atmospheric and Oceanic Sciences*, *20*(1), 193–206. https://doi.org/10.3319/TAO.2007.10.05.01(F3C

Yonezawa, T. (1971). The solar-activity and latitudinal characteristics of the seasonal, non-seasonal and semi-annual variations in the peak electron densities of the F2-layer at noon and at midnight in middle and low latitudes. *Journal of Atmospheric and Solar - Terrestrial Physics*, *33*, 887–907.

Yue, X., Schreiner, W. S., Lei, J., Sokolovskiy, S. V., Rocken, C., Hunt, D. C., & Kuo, Y. H. (2010). Error analysis of Abel retrieved electron density profiles from radio occultation measurements. *Annales de Geophysique*, *23*, 217–222.

Zeng, Z., Burns, A., Wang, W., Lei, J., Solomon, S., Syndergaard, S., et al. (2008). Ionospheric annual asymmetry observed by the COSMIC radio occultation measurements and simulated by the TIEGCM. *Journal of Geophysical Research*, *113*, A07305. https://doi.org/10.1029/2007JA012897

Zhang, M.-L., Liu, L., Wan, W., & Ning, B. (2014). An update global model of hmF2 from values estimated from ionosonde and COSMIC/FORMOSAT-3 radio occultation. *Advances in Space Research*, *53*(3), 395–402. https://doi.org/10.1016/j.asr.2013.11.053

Zhao, X., Ning, B., Liu, L., & Song, G. (2014). A prediction model of short-term ionospheric foF2 based on AdaBoost. *Advances in Space Research*, *53*(3), 387–394. https://doi.org/10.1016/j.asr.2013.12.001

Zhelavskaya, I. S., Spasojevic, M., Shprits, Y. Y., & Kurth, W. S. (2016). Automated determination of electron density from electric field measurements on the Van Allen Probes spacecraft. *Journal of Geophysical Research: Space Physics*, *121*, 4611–4625. https://doi.org/10.1002/2015JA022132